Front. Phys., 2012, 7(6): 649–669
DOI 10.1007/s11467-012-0251-2

REVIEW ARTICLE

Generation and expansion of laser-induced plasma as a spectroscopic emission source

Jin Yu (俞进)†, **Qianli Ma** (马千里), **Vincent Motto-Ros, Wenqi Lei** (雷文奇)
Xiaochun Wang (王晓纯), **Xueshi Bai** (白雪石)

Université de Lyon, F-69622, Lyon, Université Lyon 1, Villeurbanne, CNRS, UMR5579, LASIM, France
E-mail: †jin.yu@univ-lyon1.fr
Received March 1, 2012; accepted March 28, 2012

Laser-induced plasma represents today a widespread spectroscopic emission source. It can be easily generated using compact and reliable nanosecond pulsed laser on a large variety of materials. Its application for spectrochemical analysis for example with laser-induced breakdown spectroscopy (LIBS) has become so popular that one tends to forget the complex physical and chemical processes leading to its generation and governing its evolution. The purpose of this review article is to summarize the backgrounds necessary to understand and describe the laser-induced plasma from its generation to its expansion into the ambient gas. The objective is not to go into the details of each process; there are numerous specialized papers and books for that in the literature. The goal here is to gather in a same paper the essential understanding elements needed to describe laser-induced plasma as results from a complex process. These elements can be dispersed in several related but independent fields such as laser–matter interaction, laser ablation of material, optical and thermodynamic properties of hot and ionized gas, or plasma propagation in a background gas. We believe that presenting the ensemble of understanding elements of laser-induced plasma in a comprehensive way and in limited pages of this paper will be helpful for further development and optimized use of the LIBS technique. Experimental results obtained in our laboratory are used to illustrate the studied physical processes each time such illustration becomes possible and helpful.

Keywords laser ablation, laser-induced plasma, plasma propagation, plasma diagnostics, plasma emission, laser-induced breakdown spectroscopy (LIBS)

PACS numbers 52.25.Kn, 52.25.Os, 52.38.Dx, 52.38.Mf, 52.50.Jm, 52.50.Lp, 52.70.Kz

Contents

1 Introduction 650
2 Plasma generation during laser ablation 651
2.1 Absorption of laser radiation and relaxation of electronic excitation 652
2.1.1 Absorption and electronic excitation relaxation in crystalline materials 653
2.1.2 Absorption and electronic excitation relaxation in molecular solids 654
2.2 Mechanisms and modeling of plasma generation during laser ablation 656
2.2.1 Absorption of laser radiation and material vaporization from the target 656
2.2.2 Expansion of the evaporated material plume and plasma formation 657
3 Expansion of the plasma into the background gas 659
3.1 Absorption of laser radiation by vapor plume and shocked background 660
3.1.1 Absorption by inverse bremsstrahlung 660
3.1.2 Single photon ionization of excited states 661
3.1.3 Relative contributions of IB and PI and the total absorption coefficient 661
3.2 Laser-supported absorption waves 662
3.2.1 Laser-supported combustion wave 662
3.2.2 Laser-supported detonation wave 662
3.2.3 Laser-supported radiation wave 662
3.2.4 Transition between LSAW regimes: Effect of irradiance and wavelength 663
3.3 Effect of the LSAW on the propagation of the plasma into the background 664
3.3.1 Early stage of plasma expansion 664

© Higher Education Press and Springer-Verlag Berlin Heidelberg 2012

3.3.2 Expansion behavior at longer delays 665
4 Conclusions 667
References and notes 667

1 Introduction

Laser-induced breakdown is a well-known phenomenon which leads to a strongly ionized gas commonly named laser-induced plasma (LIP). Such plasma occupies a particular place in the scales of temperature and density for plasma as shown in Fig. 1 [1]. Using typical nanosecond pulsed laser with fluence in the order of 10 J/cm^2 and corresponding irradiance in the order of 10 GW/cm^2, initial temperature in the range of 10^4 to 10^5 K and initial electron density of 10^{17} to 10^{19} cm^{-3} can be typically reached in an LIP [2]. Excitation energy in the order of several to tens of eV is typically available allowing a large number of processes to occur for particles constituent of the plasma, ions, atoms as well as molecules and clusters. Such processes include absorption/emission, ionization/electron capture, and dissociation/formation of molecule, cluster and nanoparticle. In addition to primary interest as a convenient way for easy plasma production with commercially available laser, LIP represents an alternative to simulate what happens in various inaccessible and/or harmful environments such as the ionosphere, the interstellar space or the solar corona. In the presence of laser radiation, such plasma can be characterized by the energy scale, $kT \lesssim h\nu \lesssim I_p$, involving the thermal energy kT of the plasma, the energy of laser photon $h\nu$, and the ionization potential of the particles in the plasma I_p. The plasma appears therefore as a hot and ionized gas with optical absorption and demission properties sensitively dependent on its thermodynamic state. The last is in turn influenced by the radiative processes in the plasma. Strongly nonlinear processes take place in the plasma, which determine its hydrodynamic, optical as well as chemical behaviors. Such medium situates thus between hot plasma and cold gas and its description requires disciplines including atomic and molecular physics, thermodynamics, hydrodynamics, nonlinear optics, spectroscopy and also photochemistry.

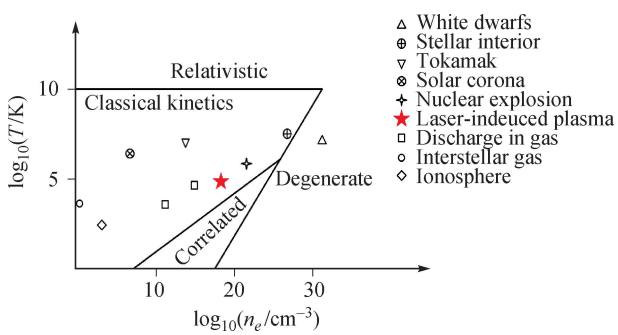

Fig. 1 Position occupied by laser-induced plasma in the scales of temperature T and electron density n_e, with respect to those occupied by other types of plasma (adapted from Ref. [1].).

Besides the fundamental interests, applications of LIP have been recently more and more attractive, especially with laser-induced breakdown spectroscopy (LIBS) [3–8]. Growing interest in spectrochemical application of LIBS is due to the unique advantages of the technique including easy sample preparation, capacity of non-contact and remote measurement, instantaneous response for multi-elemental identification and analysis and possibility of precisely localized (micro) surface analysis. Initially demonstrated in the early 60's shortly after the invention of the laser [9, 10], LIBS was first applied in detection of hazardous gas and vapors in air at Los Alamos in 1980's [11]. Further development of the technique turned to very practical problems, such as monitoring environmental contaminations, industrial applications for control of material processing, and sorting of materials or wastes [12, 13]. More specific needs from security and homeland defense trigger investigation of LIBS application in detection and analysis of explosives [14] and bacteria [15, 16]. Versatility of the technique also leads to its use for biomedical samples [17] and agriculture products [18]. The capability of LIBS to perform remote detection enables its application in the nuclear industry [19]. The integration by the NASA of a module of LIBS in the Mars exploration rover "Curiosity" for analysis of the soil of Mars highlights the application of LIBS for space exploration [20, 21].

Fast development of the LIBS technique and its application in a wide range of domains make laser-induced plasma today so popular that one tends to forget the complex physical and chemical processes leading to its generation and governing its evolution. Further development of the technique is however crucially dependent on a deeper understanding and more detailed description of the mechanisms involved in the generation and the evolution of the plasma. Compared to the established element analytical techniques such as inductively coupled plasma atomic emission spectroscopy or mass spectrometry (ICP-AES or ICP-MS), LIBS is still currently considered as an emergent technique in despite of its demonstrated potentials. Its sensitivity, the precision and the accuracy of its measurements, or in one word, its performance for quantitative analysis, are expected to be significantly improved [22, 23]. Back to the fundamental of the laser-induced plasma for a better understanding and description of the phenomenon is currently considered by the international LIBS community as a necessary approach to significantly accelerate the maturation of the technique.

In this review we will summarize the physical backgrounds necessary to understand and describe the laser-induced plasma from its generation to its propagation into the ambient gas. Our objective here is not to go

into the detail of each process, which has been treated in many other specialized papers and books. The focus of this paper is the understanding of the complex process leading to laser-induced plasma. The basic understanding elements can be dispersed in several related but independent fields such as laser-matter interaction, laser ablation, optical and thermodynamic properties of hot and ionized gas, and plasma propagation into a background gas. We believe that the presentation of the ensemble of understanding elements in a comprehensive way and in limited pages of this paper will be helpful for further development and optimized use of the LIBS technique. Often LIBS developers or users are faced with a large variety of materials to be analyzed (metals, dielectrics, organics, or biological materials) and wide possible choices for ablation configuration concerning either laser parameters (fluence, wavelength, pulse duration) or background (gas nature or pressure). Only a good understanding of the physics behind LIBS allows for a correct use of the technique and adapting it to each specific application. As we mentioned above, the majority of plasmas for spectroscopic applications are generated using a nanosecond pulsed laser because of the practical convenience of such laser source. We limit therefore our consideration in this paper to the physics of the interaction between matter and a nanosecond laser pulse. Such limitation excludes a large range of extremely important processes of actual focus for a broad area of research. Interested readers can gain an insight into the interaction of ultra-short laser pulse with matter through related review papers or books [24, 25].

In Section 2 of the paper, we will provide a description of the process of laser ablation, which is responsible for plasma generation. The generated plasma subsequently expands into the background gas. For nanosecond-laser ablation, the early stage of expansion of the plasma takes place in the presence of the laser radiation. We will discuss in Section 3, the mechanisms of plasma propagation driven by the interaction between the plasma and the laser radiation together with the coupling with the background gas. Although theoretical models and experimental results from the literature will be used in this paper to provide the state of the art of our actual comprehension of laser-induced plasma, experimental results obtained in our laboratory will also be presented to illustrate the studied physical processes each time such illustration becomes possible and useful.

2 Plasma generation during laser ablation

Laser-induced plasma produced during pulsed laser ablation corresponds to the mass of target material removed consequently to absorption of the laser radiation by the target. Several steps can be distinguished to understand and describe the generation of ablation plasma and its subsequent evolution in the background gas. As illustrated in Fig. 2, the process starts at the instant when the leading edge of the laser pulse reaches the target surface. Energy of the incident laser pulse is first absorbed by material touched by the laser pulse, which induces microscopic as well as macroscopic changes in the material. In particular, if the fluence or the irradiance of the laser pulse exceeds the threshold of ablation, phase transitions occur in the irradiated volume leading to the generation of a vapor. Such vapor can be neutral or

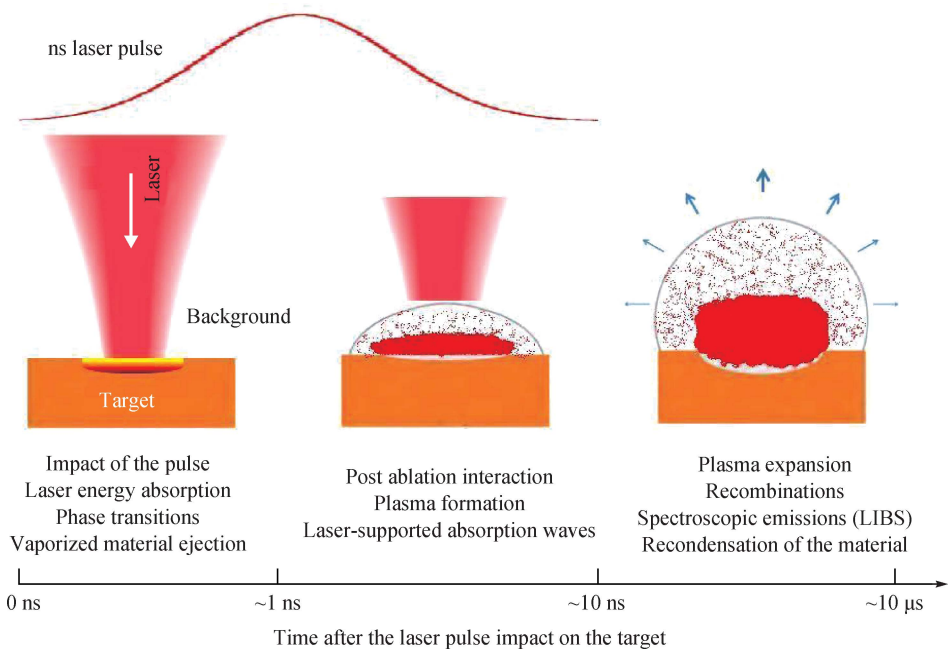

Fig. 2 Sequential processes in the generation and evolution of a plasma induced a nanosecond laser pulse with a typical timescale for the development of the sequence.

ionized and in the case of nanosecond or longer duration pulse ablation, it interacts with the incoming laser pulse. Its high density and temperature and initial free electrons in it permit it to absorb efficiently the laser energy and get highly ionized. A plasma is thus generated above the target surface, leaving behind it a crater. The plasma expands into the background gas and interacts strongly with it. Since the laser pulse may still present during the early stage of the plasma expansion, the so-called laser-supported absorption wave (LSAW) dominates the propagation of the plasma into the background. After the termination of the laser pulse, the resulting system continues to expand into the background. Relaxation processes take place in the plasma including the spectral emission from the plasma, which is the basis of the LIBS technique. The plasma finally condenses itself. A typical timescale of the development of the sequential processes during the lifetime of the plasma is also indicated in Fig. 2. In the present Part of the paper we will describe the formation of the plasma. The expansion of the plasma will be the subject of Section 3. Attention will be focused on the understanding of the involved physical processes. Useful theoretical models and formulas will also be introduced.

2.1 Absorption of laser radiation and relaxation of electronic excitation

Absorption of laser radiation by material and relaxation of electronic excitation are the key processes in laser ablation. Such processes depend on the microscopic interaction mechanisms between the laser radiation and the matter, as well as the macroscopic property of the material. Since for LIBS applications, laser ablation can concern matter in any state of gas, liquid or solid phases, a complete review of laser-induced plasma for LIBS should discuss specifically each case. Such review represents obviously a huge work that will not be the purpose of this paper. In the following instead, we will focus on solid materials, which include usual solid state or crystalline materials (metals or inorganic dielectrics) and so-called molecular solids (polymers and some biological materials). The study of laser-induced plasma from these materials already concerns such large range of fundamental processes, the understating of which also helps us to deal with laser-induced breakdown in gas and in liquid although specific features have to be included in the consideration for each specific state of the matter.

Optical property of a material can be influenced by the characteristics of the laser pulse. Among the most important parameters of a laser pulse, there are pulse duration (and more generally the temporal profile of the pulse), fluence and wavelength. For LIBS, Nd:YAG laser is typically used because of its reliability and efficiency for ablation on any material with easily generated harmonics from the near ultraviolet (UV) to the near infrared (IR). The typical pulse duration of a Nd:YAG laser ranges from several to tens of nanoseconds. Typical fluence used in LIBS is in the order of 10 J/cm^2 which corresponds to an irradiance of 10^9–10^{10} W/cm^2. The available wavelengths with the fundamental and the harmonics of a Nd:YAG laser are listed in Table 1 together with the corresponding photon energy.

Table 1 Available wavelengths with a Nd:YAG laser associated to harmonics generation together with associated photon energy.

Wavelength /nm	Photon energy /eV
1064	1.17
532	2.33
355	3.49
266	4.66

Attenuation of a laser beam propagating in a material medium can be described by the Beer–Lambert law [26], if the beam is propagating in the x direction and $I(x)$ is its irradiance at a position x,

$$\frac{\mathrm{d}I(x)}{\mathrm{d}x} = -\alpha \times I(x) \tag{1}$$

where the used derivative form provides a more general description and when the parameter α becomes constant and homogenous, the usual integrated Beer–Lambert law can be obtained,

$$I(x) = I_0 \exp(-\alpha x) \tag{2}$$

where I_0 is the irradiance at $x = 0$. The physics of laser–matter interaction is included in the parameter α which is the attenuation coefficient. In such global attenuation one can distinguish the contributions of absorption and scattering. In a homogenous material however, the scattering becomes negligible, and in general the parameter α is considered as absorption coefficient. Optical absorption coefficient represents one of the most important optical properties of the matter. It is obviously specific for each type of solid and for each considered material. It depends on the detailed microscopic interaction between laser radiation and matter. It is usual to consider the crystalline materials on the one hand and the molecular solids on the other hand because of the different dominant mechanisms in these two classes of solid materials.

Relaxation occurs subsequently to optical absorption leading to electronic excitation in matter, which is responsible of energy coupling between the different degrees of freedom in the matter and consequently the degradation of the material through the absorption of laser radiation. Different relaxation channels and mechanisms can be observed in crystalline materials or in molecular solids due to their distinguished microscopic structures as for optical absorption. In the following we will continue our discussion separately for crystalline materials and molecular solids.

2.1.1 Absorption and electronic excitation relaxation in crystalline materials

Band structure is a well-known concept to describe the electronic energy structure in solid state materials [27, 28]. A figure adapted from Ref. [26] can be used to illustrated electronic structure of crystalline materials (we limit ourselves here to metal and dielectric for simplicity) as shown in Fig. 3. In a pure dielectric, the valence band is filled by electrons while the conduction band is totally empty (strictly true at 0 K). Only interband transition can be responsible for optical absorption leading to the creation of an electron–hole pair. A typical value of band gap of dielectrics is that of diamond of 5.5 eV [26]. Compared to photon energies available with a Nd:YAG laser, one can see that single photon absorption is in general not possible in dielectric. Multiphoton absorption can lead to interband transition in a dielectric which becomes important when laser irradiance increases. For moderate irradiance usually encountered in LIBS, the presence of defects is crucial for optical absorption of a dielectric since they introduce energy levels inside of the band gap in such way that the electrons occupying the defect levels can be excited into the conduction band through single photon absorption. The balance between the multiphoton interband absorption and the single photon defect absorption depends on the concentration and the nature of the defaults in the crystal and the characteristics of the used laser. The calculation of the absorption coefficient α can be very complicated and depends on the specific structure of the dielectric and the characteristics of the laser pulse. The situation is quite different for metal where simple model can be used to calculate the absorption coefficient. In a metal, the highest occupied band is only half filled by the valence electrons. The Fermi level lies therefore in the middle of the band. Intraband single photon transition is possible for an electron under the Fermi level to be excited into an energy level above the Fermi level in the same energy band. The mechanisms of optical absorption in crystalline materials, dielectric and metal, can be therefore summarized by intrinsic interband or intraband transitions and transition from a defect level as illustrated in Fig. 4.

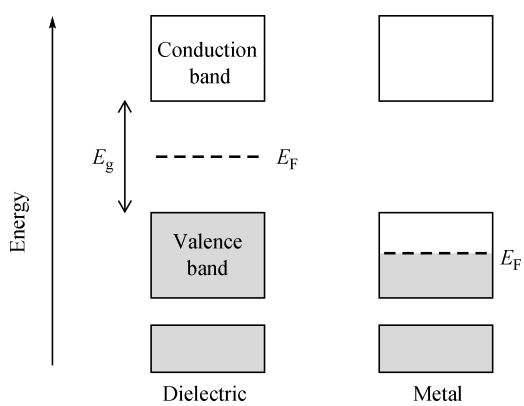

Fig. 3 Band structure in solid state materials where energy bands are separated by band gap E_g. The bands are filled with electrons up to the Fermi level E_F. Such occupation is indicated by the shading.

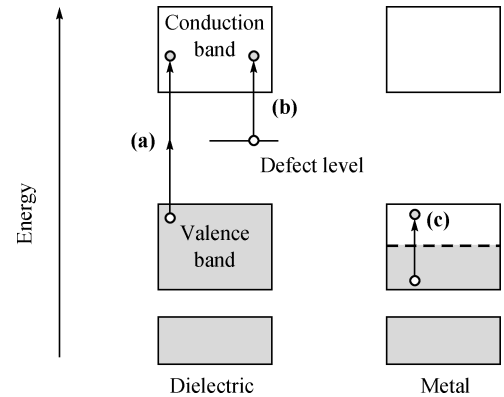

Fig. 4 Optical absorptions in crystalline materials: **(a)** Interband multiphoton absorption; **(b)** Defect transition; **(c)** Intraband absorption.

In the classical treatment of the optical response of metals with the Drude model [29], the valence electrons are treated as free electrons that interact with electromagnetic field "freely" without restoring force from the ions which form the crystalline lattice. The electrons interact with the lattice through collisions with heavy and relatively immobile positives ions. With such simple model, analytical expression of the absorption coefficient can be obtained for metal. Coupled with the Lorentz dipole oscillator model of atom, the Drude–Lorentz model describe the oscillation of a free electron induced by the AC electric field associated to a laser radiation, $\mathcal{E}(t)$, with the following equation [26]:

$$m_e^* \frac{\mathrm{d}^2 x}{\mathrm{d}t^2} + m_e^* \gamma \frac{\mathrm{d}x}{\mathrm{d}t} = -e\mathcal{E}_0 \mathrm{e}^{-\mathrm{i}\omega t} \tag{3}$$

where m_e^* is the effective mass of the electron, $\mathcal{E}_0$ the amplitude of the laser electric field and ω its pulsation. The friction coefficient γ is considered as equal to $1/\tau$, where τ is considered as the mean time between two consequent collisions between an electron and an ion. Compared to the standard Lorentz model of the atom, in Eq. (3) the term due to the restoring force of the ion on the electron is set to zero ($\omega_0 = 0$). The solution of this equation for the displacement of the electron, x, leads to the relative permittivity of the metal. A characteristic parameter is introduced to describe the optical response of the metal, ω_p, the plasma frequency which is defined by

$$\omega_p = \sqrt{\frac{n_e e^2}{\varepsilon_0 m_e^*}} \tag{4}$$

where ε_0 is the permittivity of the free space, n_e stands for the free electron number density, which is in the order of 10^{22} to 10^{23} cm^{-3} for metals [26]. The plasma frequency is a key parameter for the optical property of

a metal. A radiation with $\omega < \omega_p$ is reflected by the surface of the metal with a reflectivity R close to 1. The absorption coefficient α can be thus expressed as a function of ω_p, τ, and ω,

$$\alpha = \sqrt{\frac{2\omega_p^2 \tau \omega}{c^2}} \tag{5}$$

From α, one can define the skin depth, δ, which represents the distance under the target surface where the laser field strength decreases to e^{-1} of the incident strength.

$$\delta = \frac{2}{\alpha} = \sqrt{\frac{2c^2}{\omega_p^2 \tau \omega}} \tag{6}$$

The value of α for metals is in the order of 10^6 cm^{-1}, which leads to a skin depth in the order of 10 nm. In a real metal, the simple free-electron behavior is modified by a number of secondary effects, such as interband transitions [30]. Measured reflectivity and absorption coefficient for Al and Cu are shown in Fig. 5 reproduced from Ref. [30]. Extensive data for R and α are available in the literature [30, 31].

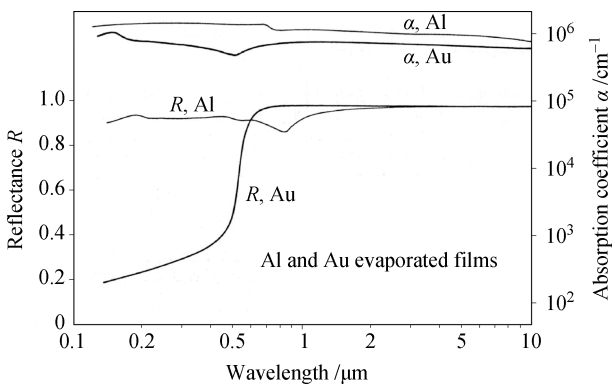

Fig. 5 Measured absorption coefficient α and reflectivity R for Al and Au as a function of wavelength. Reproduced from Ref. [30], Copyright © 1998 Springer-Verlag.

It is however important to remark that the optical properties of a metal are sensitively dependent on its temperature. In particular, the reflectivity drastically decreases with the increasing temperature basically because of the increasing electron–phonon collision frequency with the temperature [32, 33]. During laser ablation of a metal, the absorption of laser radiation by the target raises its temperature. Such a rise in turn induces a lower reflectivity and thus a stronger energy absorption in the metal. A detailed treatment of laser ablation needs to take into account such nonlinear and dynamic processes.

An excited electron is in contact with a large number of particles in solid, ions which form the lattice, other free electrons, or the hole which has been created at the same time as the excited electron. The energy stored by the electron can be efficiently relaxed into other forms of excitation. Radiative relaxation corresponds to electron–hole recombination. It is the inverse process of optical absorption. The ratiative lifetime of an electron–hole pair is in the nanosecond rang, much longer than the timescales of electron–electron collision and electron–lattice coupling. Collision time between free electrons in a solid can be very short in the range of 10^{-14} s due to high free carrier density [26]. Coupling with the lattice can be considered as electron–phonon coupling, and electron scattering takes place on a timescale as short as 10^{-12} s [30]. These different timescales determine the principal ways of the relaxation of an excited electron through non radioactive processes, i.e., electron–electron and electron–phonon couplings. For a nanosecond pulse, these relaxation processes occur instantaneously and transfer the absorbed optical energy into the thermal energy of the free electron and then that of the lattice. The laser pulse acts therefore as a source of heat which, during its propagation in to a solid target, induces a rise of temperature in it. The consequence can be the melting, then the evaporation of the target material, if the corresponding thresholds in fluence or in irradiance are successively reached.

2.1.2 Absorption and electronic excitation relaxation in molecular solids

Molecular solids can include a wide range of solid state materials such as polymers or some biological materials frequently concerned by LIBS application. The structure of these materials is characterized by assemblage of long molecular chains with strong covalent bonds inside. At the same time, the molecules of different chains interact weakly, in such way that the optical property of the material is predominantly determined by that of the individual molecules which compose the material [34]. Molecular optical spectra are generally divided into three spectral regions: the far-infrared spectra ($\lambda > 100$ μm), the infrared spectra ($\lambda \sim 1$–100 μm) and the visible and ultraviolet spectra ($\lambda < 1$ μm), respectively corresponding to transitions between the rotational, vibrational and electronic states of the molecule. For laser ablation, only visible and ultraviolet spectra are concerned, which affect the electronic state of the molecule.

Due to the coupling between the electronic and vibrational states of a molecule, a transition between two electronic states is always accompanied by a change in its vibrational state. The concept of vibronic transition is used to describe vibrational–electronic transitions in a molecule. The disconnection of the motions between the electrons and the nuclei permits to understand molecular vibrational–electronic spectra with the aid of the configuration diagrams as shown in Fig. 6 for a simple diatomic molecule. According to the Franck–Condon principle, vibrational–electronic transitions occur verti-

cally between potential energy curves, at a constant internuclear distance, and become more probable when the overlap between the vibrational wave functions between the lower and the upper electronic states is maximal. This means that a typical optical absorption occurs between the vibrational equilibrium position in the ground electronic state and the return point in the vibrational potential of the excited electronic state as shown in Fig. 6 at the internuclear distance $r = r_1$. This distance does not correspond to the vibrational equilibrium distance in the excited electronic state, rapid non radiative relaxation occurs for the molecule to reach its new vibrational equilibrium in the electronic excited state, r_2, as shown in Fig. 6 by a dashed arrow.

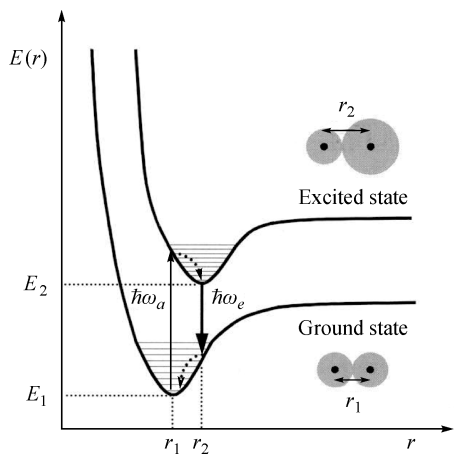

Fig. 6 Energy-level diagram for the ground and an excited state of a diatomic molecule as a function the internuclear distance r. Optical absorption and emission as well as relaxations of vibrtaional energy are indicated by arrows. Reproduced from Ref. [26], Copyright © 2010 Oxford University Press.

In a molecular solid, an optically excited molecule is in close contact with other molecules, the vibrational relaxation takes place in a very short timescale of less than 1 ps [26]. And the released energy ends up as heat. The molecule in its new vibrational equilibrium position emits then a fluorescence photon and returns back to its ground electronic state. Again the Franck–Condon principle leads its departure from the vibrational equilibrium position in the ground electronic state and non radiative relaxation occurs as for absorption. The typical fluorescence lifetime is about 1 ns which is much longer than the non radiative relaxation. One encounters here a similar situation as in the case of nanosecond laser ablation of metal, the laser pulse acts as a heat source that induces a rise of the temperature in the irradiated material through the cycle of absorption-relaxation. Such temperature rise in molecular solid can lead to dissociation of a molecule from its ground electronic state when its vibrational state is so highly excited to break the bond.

Unlike the case of metal, other bond breaking mechanisms are possible for molecular solids. In particular, an optical absorption can directly bring a molecule into a dissociative electronic excited state. Expulsive force between the two atoms breaks the bond and renders them free each other. Such mechanism can directly evaporate fragments from a molecular solid without temperature rise in the target. This non thermal process is called photochemical process. A threshold is often observed for photochemical process with respect to laser irradiance or laser wavelength, and depends on the energy potential diagram of the molecule. Different configurations of optical dissociation can be resumed in Fig. 7 reproduced from Ref. [35].

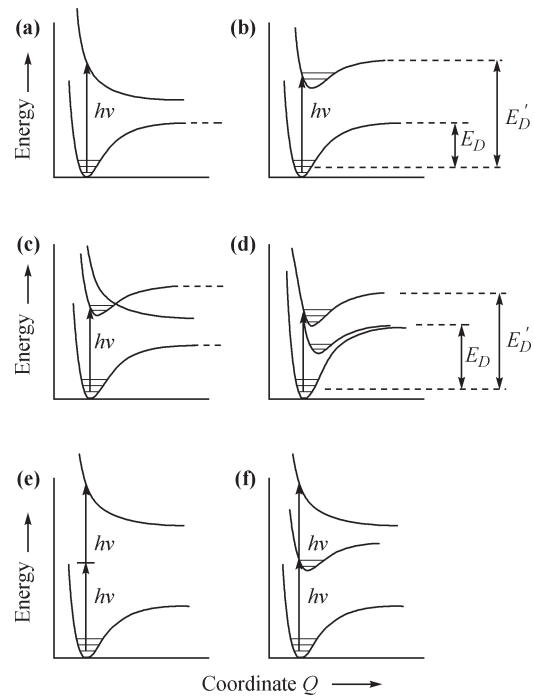

Fig. 7 Potential energy curves for the ground and excited states of a diatomic molecule as a function the internuclear distance. Different configurations of optical dissociation are shown. Reproduced from Ref. [35], Copyright © 2000 Springer-Verlag.

When the excitation photon energy exceeds the molecule dissociation energy, E'_D [Figs. 7(a) and (b)], a single photon absorption can lead to molecule dissociation because either the excited electronic state is dissociative [Fig. 7(a)] or the vibrational state in the excited electronic state is over the dissociation energy [Fig. 7(b)]. Dissociation takes place quickly in a timescale of typically 10^{-14} to 10^{-13} s. When the excitation photon energy is below the molecule dissociation energy, the molecule can still be dissociated. Figures 7(c) and (d) show the cases where a single photon absorption brings the molecule to an excited state which either crosses a dissociative potential curve [Fig. 7(c)] or another excited state with lower dissociation energy, E_D [Fig. 7(d)]. In Figs. 7(e) and (f), coherent and non coherent two-photon absorptions are shown for the excitation of a molecule into its dissociative state.

2.2 Mechanisms and modeling of plasma generation during laser ablation

After discussing in Section 2.1 the principal mechanisms of optical absorption and electronic excitation-relaxation in solid state materials, we will study in this Section the mechanisms leading to the generation of a plasma during laser ablation. It is clear that the phenomenon starting from the absorption of laser radiation by solid material and ending by the formation of a plasma implies a very complex process. Simplified models are always useful to get insights of essential mechanisms involved and their interrelationship, although complicated numerical codes can take into account all significant processes in laser ablation of solid materials with a high degree of complexity. In general, nanosecond laser ablation of solid materials is treated according to the three following simplified pictures: photothermal ablation, photochemical ablation and photophysical ablation [35]. In photothermal ablation, the electronic excitation due to photon absorption is thermalized in a very short timescale. And accumulated heating can lead to thermally activated lattice degradation or bond breaking. On the other hand, in photochemical process, the electronic excitation results in direct lattice degradation or bond breaking without heating of the material. When both thermal and nonthermal processes play a role, photophysical process is more suitable to describe the phenomenon. According to the discussions in Section 2.1 we can see that the nanosecond ablation of metal is a typical case where the photothermal process dominates. A typical scanning electronic microscope (SEM) image of a crater left by an infrared pulse on an Al target is shown in Fig. 8. We can observe polished bottom surface of the crater suggesting solidification of molten metal after the laser pulse. The ablation of molecular solids however can be very complex, implying thermal or non thermal processes [34, 36]. Generally applicable model does not exist today and the discussions is still going on concerning the mechanism of polymer ablation 30 years after the first reports on the phenomenon in 1982 [37]. In the following we will focus on the case of ablation of a metallic target and present a description with a model based on the photothermal process in order to get insight of the process leading the generation of vapor plasma following the absorption of a laser pulse. For this purpose, we choose to follow the paper published by Bogaerts *et al.* in 2003 [38]. In this paper and in a series of papers published by the same authors between 2003 and 2006, the authors present in a comprehensive way their model and numerical results on ablation of a pure copper target by a nanosecond pulse and the subsequent propagation of the generated plasma into the background gas [38–41]. With this basic one dimension model, we will follow step by step the development of the complex process which leads to the final formation of a plasma consequently to the absorption of a laser pulse by the target.

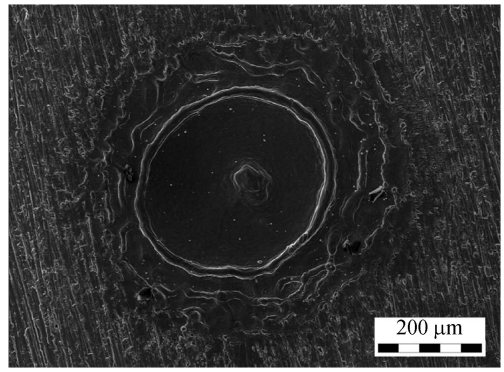

Fig. 8 SEM image of a crater caused by a series of 10 infrared pulses (1064 nm) on the surface of an aluminum target.

2.2.1 Absorption of laser radiation and material vaporization from the target

Input parameters of the model described in Ref. [38] are provided in Table 2.

Table 2 Input parameters with definitions and values used in the presented model adapted from Ref. [38]. For the references for these data see Ref. [38].

Parameters	Values for Cu
Thermal conductivity, κ ($\mathrm{W \cdot m^{-1} \cdot K^{-1}}$)	380 (solid), 170 (liquid)
Specific heat, C_p ($\mathrm{J \cdot kg^{-1} \cdot K^{-1}}$)	420 (solid), 494 (liquid)
Mass density, ρ ($\mathrm{kg \cdot m^{-3}}$)	8960 (solid), 8000 (liquid)
Absorption coefficient, α ($\mathrm{m^{-1}}$)	7.44×10^7
Reflectivity, R	0.34
Melting point, T_m (K)	1358
Boiling point, T_b (K)	2836
Heat of fusion, ΔH_{sl} (J/mol)	1.3×10^4
Heat of vaporization, ΔH_{lv} (J/mol)	3.048×10^5
First ionization potential, IP_1 (eV)	7.73
Second ionization potential, IP_2 (eV)	20.29
Electronic work function, ϕ (eV)	4.5

Following the impact of a laser pulse on the target surface and as a consequence of the absorption of laser energy, the temperature in the target rises in the volume touched by the laser pulse. Because the penetration depth of the laser pulse in the order of 10 nm ($1/\alpha$) is much smaller than the size of the focused laser beam on the surface of the target of typically 100 μm, one-dimension heat conduction equation is used to deduce the temperature profile, $T(x,t)$, in the target during laser pulse propagation in it:

$$\frac{\partial T(x,t)}{\partial t} = \frac{\partial}{\partial x}\left[\frac{\kappa}{C_p \rho}\frac{\partial T(x,t)}{\partial x}\right] + \frac{\alpha}{C_p \rho} I(x,t) \tag{7}$$

where x is the distance in the target from the target surface. Other used parameters are defined in Table 2. The

second member of the right side of Eq. (7) represents the energy source by absorption of laser energy. $I(x,t)$ stands for the laser irradiance as a function of time and position in the target. It can be written by including the surface reflection in Eq. (2):

$$I(x,t) = I_0(t)\exp(-\alpha x)(1-R) \tag{8}$$

where $I_0(t)$ is the incident laser irradiance. A Gaussian-formed pulse is taken with 10 ns duration at full width at half maximum (FWHM). In the model, α and R are considered as constants during the ablation process, which is obviously a simplification.

When the temperature rises in the target, melting takes place inside the target where the temperature reaches the melting point. The melting starts at the surface and the melt front propagates inside the target. When the temperature further rises, vaporization becomes significant on the surface. The vapor pressure, $p_{\rm vap}$, is calculated from the surface temperature, T_s, by the Clausius–Clapeyron equation:

$$p_{\rm vap}(T_s) = p_0 \exp\left[\frac{\Delta H_{lv}(T_s - T_b)}{RT_sT_b}\right] \tag{9}$$

where $p_0 = 1$ atm, R the gas constant and other parameter are defined in Table 2. From the vapor pressure, the vapor density at the surface, $p_{{\rm vap},s}$ can be calculated using the ideal gas law:

$$\rho_{{\rm vap},s} = \frac{p_{\rm vap}}{k_{\rm B}T_s} \tag{10}$$

where $k_{\rm B}$ is the Boltzmann constant. Further assuming that the vapor atoms leaving the surface follow the one-dimensional Maxwellian velocity distribution, the mean velocity of the vapor can be deduced:

$$v_{{\rm vap},s} = \sqrt{\frac{2k_{\rm B}T_s}{\pi m}} \tag{11}$$

where m represents the mass of a Cu atom.

The numerical results of the model concerning the evolution of the temperature in the target and the generation of a vapor at the target surface can be presented using the several figures reproduced from Ref. [38]. In Fig. 9, the temporal profile of the incident laser pulse is plotted together with the laser irradiance arriving at the sample surface. We can observe a drop of laser irradiance arriving on the sample surface at around 10 ns due to the formation of a vapor over the target surface and its screening by the laser pulse. The temperature profile in the target as a function of the time after the arrival of the laser pulse is shown in Fig. 10. We see in the figure how the melt front propagates inside the target. The obtained vapor density, vapor velocity and vapor temperature at the surface are used as inputs for the calculation for the expansion of the vapor in the next step of the model.

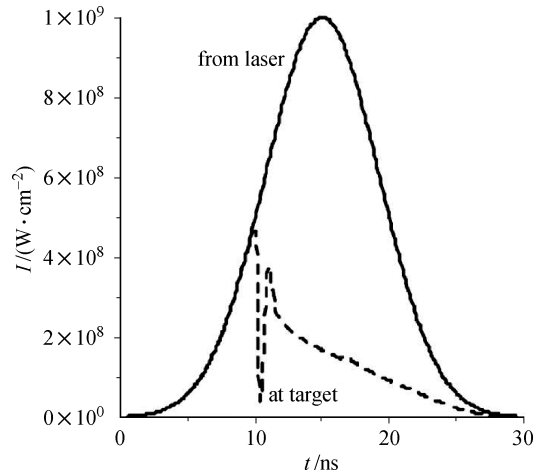

Fig. 9 Temporal profile of the irradiance of the incident laser pulse (*solid line*) and the laser irradiance arriving on the target surface. Reproduce from Ref. [38], Copyright © 2003 Elsevier.

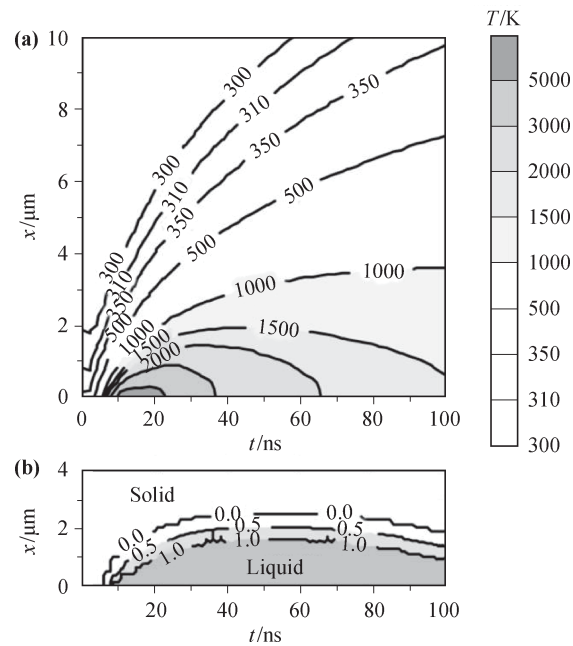

Fig. 10 Temperature profile inside of the target as a function of the time after the arrival of the laser pulse **(a)** and the contour of liquefaction in the target **(b)**. Reproduced from Ref. [38], Copyright © 2003 Elsevier.

2.2.2 Expansion of the evaporated material plume and plasma formation

The produced vapor expands into the background. The simplest configuration is a vacuum background. The specificity of a background gas with a relative high pressure will be discussed in Section 3 of this paper. Here we first take interest in the expansion into the vacuum, which is representative of the expansion behavior of a plasma at short delays even into a background gas. The expansion of the evaporated material into vacuum is described by the Euler equations of hydrodynamics which

express the conservation of the mass, the momentum and the energy:

$$\frac{\partial \rho}{\partial t} = -\frac{\partial(\rho v)}{\partial x} \tag{12}$$

$$\frac{\partial(\rho v)}{\partial t} = -\frac{\partial}{\partial x}(p + \rho v^2) \tag{13}$$

$$\frac{\partial}{\partial t}\left[\rho\left(E + \frac{v^2}{2}\right)\right] = -\frac{\partial}{\partial x}\left[\rho v\left(E + \frac{p}{\rho} + \frac{v^2}{2}\right)\right] + \alpha_{IB} I_{\text{laser}} - \varepsilon_{\text{rad}} \tag{14}$$

where ρ is the mass density of the vapor, ρv is the momentum, ρE is the internal energy density, $\rho v^2/2$ is the kinetic energy density, and p the local pressure. The source term in the right-hand side of Eq. (14), α_{IB} is due to the absorption of laser radiation by the expanding vapor through the inverse bremsstrahlung [42]. We will go back to this topic more in detail in Section 3 of the paper. ε_{rad} represents the amount of energy lost by the vapor through bremsstrahlung emission. Assuming that the electrons are characterized by a Maxwellian velocity distribution, ε_{rad} can be expressed as [43]:

$$\varepsilon_{\text{rad}} = \sqrt{\frac{2\pi k_{\text{B}} T}{3m_e}} \frac{32\pi e^6}{3hm_e c^3} n_e (Z_1^2 n_{Z_1} + Z_2^2 n_{Z_2}) \tag{15}$$

where m_e and e are electron mass and charge, n_e, n_{Z_1} and n_{Z_2} represent the number densities of electrons, Cu^+ and Cu^{2+} ions, and $Z_1 = 1$ and $Z_2 = 2$ refer to the charges of singly and doubly ionized ions.

Assuming that the vapor follows the ideal gas law, the pressure and the internal energy density can be expressed as follows [44]:

$$p = (1 + x_e)\frac{\rho k_{\text{B}} T}{m} \tag{16}$$

$$\rho E = \frac{\rho}{m}\left[\frac{3}{2}(1 + x_e)k_{\text{B}}T + IP_1 x_{Z_1} + (IP_1 + IP_2)x_{Z_2}\right] \tag{17}$$

where x_e, x_{Z_1} and x_{Z_2} are the fraction of electrons, singly and doubly charged ions of Cu in the vapor, respectively. Considering the vapor is in local thermodynamic equilibrium (LTE) [45] because of high electron density in the plasma, which assures many collisions between different species in the vapor. Such consideration can be verified by the McWhirter criterion requiring a minimum electron density typically in the order of 10^{16} cm^{-3}. For a plasma in LTE, all species of particles in the vapor, electrons, atoms and ions are in thermal equilibrium and they are characterized by a common temperature. In this case, the Saha–Eggert equation can be used to describe the ionization degree of the vapor:

$$\frac{x_e x_{Z_1}}{x_0} = \frac{1}{n_{\text{vap}}}\left(\frac{2\pi m_e k_{\text{B}} T}{h^2}\right)^{3/2} \exp\left(-\frac{IP_1}{k_{\text{B}}T}\right) \tag{18}$$

$$\frac{x_e x_{Z_2}}{x_{Z_1}} = \frac{1}{n_{\text{vap}}}\left(\frac{2\pi m_e k_{\text{B}} T}{h^2}\right)^{3/2} \exp\left(-\frac{IP_2}{k_{\text{B}}T}\right) \tag{19}$$

where $n_{\text{vap}} = \rho/m$ represents the total vapor number density, and x_0 the fraction of neutral Cu atoms in the vapor. In typical ablation plasma, we assume that only single and double ions are possible. The matter and charge conservations lead to

$$x_0 + x_{Z_1} + x_{Z_2} = 1 \tag{20}$$

$$x_{Z_1} + 2x_{Z_2} = x_e \tag{21}$$

Very close to the target surface, the main source of ions and electrons is the thermionic emission from the hot surface [46]. The ionization degree of the vapor is described by the Langmuir–Saha equation:

$$\frac{x_{Z_1}}{x_0} = \exp\left(\frac{\phi - IP_1}{k_{\text{B}}T_s}\right) \tag{22}$$

where ϕ is the electronic work function defined in Table 2.

Numeric results are shown in Figs. 11 and 12 for a delay of 15 ns and 100 ns respectively. We can see in Fig. 11 that 15 ns after the arrival of the laser pulse on the target, a vapor is observed over the surface up to a

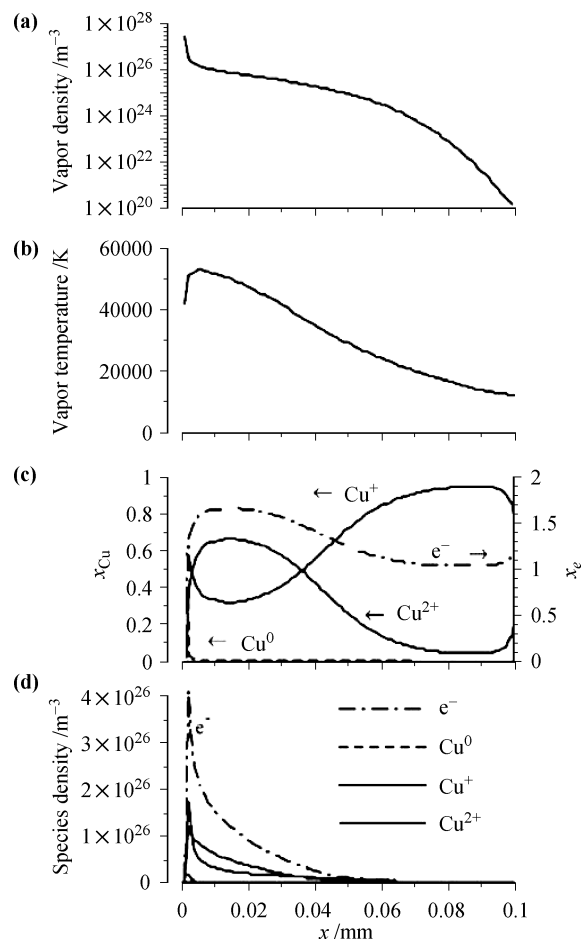

Fig. 11 Calculated vapor density **(a)** temperature distribution **(b)**, fractions of Cu atoms, Cu^+ and Cu^{2+} ions and electrons **(c)**, and species number density as a function of the distance from the target surface at a delay of 15 ns. Reproduced from Ref. [38], Copyright © 2003 Elsevier.

distance of 100 μm with a temperature in the range from 20 000 K to 60 000 K. This temperature is much higher than the boiling temperature of 2836 K of copper. Such high temperature shows the efficiency of the heating of the metallic vapor due to the laser radiation. The vapor is almost totally ionized with an electron density in the order of 10^{20}cm^{-3}. The observed electron density justifies the LTE condition in the plasma. At a longer delay of 100 ns (Fig. 12), the expansion of the plasma leads to an extension of the plasma up to 2.5 mm, a more homogenous temperature of around 20000 K, and an ionization degree which remains always very high with an electron density in the order of 10^{18}cm^{-3}. Although the propagation of the plasma is studied here in the vacuum, it provides actually a good approximation at short delays of the description of the formation of a plasma and its expansion into a background gas even at relative high pressure of one atmosphere. The behavior of the plasma at longer delays and the specificities related to a high pressure background gas will be the subjects of Section 3 of the paper.

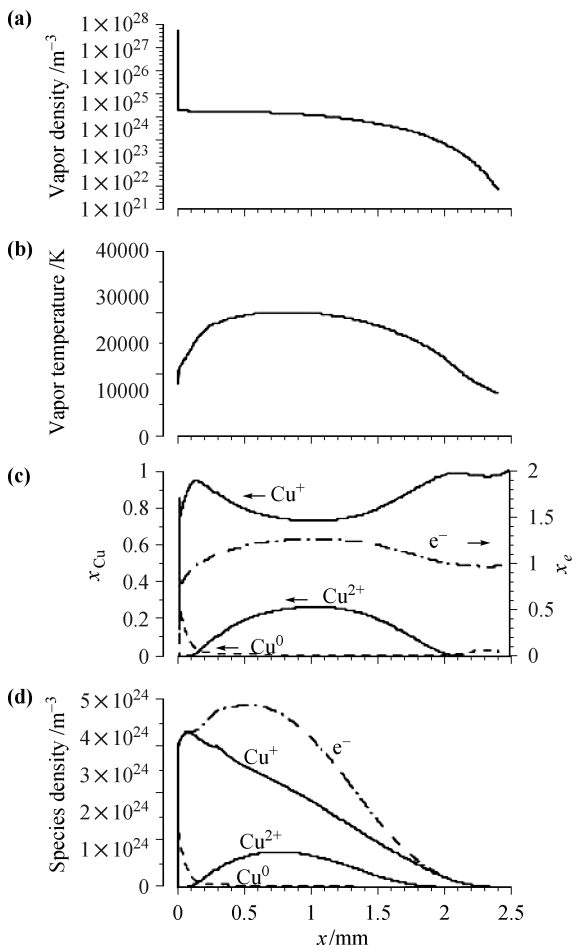

Fig. 12 Calculated vapor density **(a)** temperature distribution **(b)**, fractions of Cu atoms, Cu^+ and Cu^{2+} ions and electrons **(c)**, and species number density as a function of the distance from the target surface at a delay of 100 ns **(d)**. Reproduced from Ref. [38], Copyright © 2003 Elsevier.

3 Expansion of the plasma into the background gas

In the most of the cases, an LIBS measurement is performed in a background gas at the atmospheric pressure, with the ambient air or an introduced gas, such as argon or helium. The property of the plasma as a spectroscopic source directly depends on its expansion behavior into a background gas at a pressure of one atmosphere, because its emission is detected during this time interval. In this part, we will discuss the main mechanisms involved in the expansion process with emphasis on the specificity due to the high pressure of the background gas.

The standard theory describing the expansion of a plasma into an ambient pressure background gas is the Sedov point-blast model [47, 48]. The basic idea of this model is that the expansion of the plasma is driven by the energy locally deposited on the target surface by the laser pulse at the initial instant. In the presence of an ambient gas, the vapor plume acts as a piston which pushes away and compresses the background gas with the propagation of a shockwave. Discontinuities appear in the vicinity of the contact boundary separating the vapor plume and the compressed (or shocked) background gas. More recent numerical simulations based on the gas-dynamic model have included diffusion around the contact boundary, which leads to a mixing zone between the vapor and the shocked background gas with a limited width in the vicinity of the boundary [40].

A specific feature of nanosecond pulsed laser ablation is however that the pulse duration is significantly longer than the initiation time of the plasma which is commonly considered the interval between the initial impact of the laser pulse on the target and the appearance of evaporated material over its surface. Using picosecond time-resolved shadowgraph imaging, the initiation time has been measured in the range of several hundred picoseconds [49]. The expanding vapor plume as well as the shocked gas can thus absorb energy from the incoming laser pulse leading to its shielding. Such shielding is especially efficient in ambient pressure background, in which the vapor plume is efficiently slowed down and confined. Thermal ionization can thus occur in the shocked gas, increasing the absorption rate of the gas. For nanosecond ablation in high background pressure, the laser energy is therefore not totally deposited on the target surface at the initial instant as assumed in the piston model. The early stage of the plasma expansion is more exactly driven by laser-supported absorption waves (LSAW) [50]. The absorption of the laser pulse by the interacting system, which can include the vapor plume and the shocked background gas, is the key point which determines the subsequent evolution of the plasma. In order to facilitate our discussions below, we use a schematic representation

adapted from Ref. [50]. of the interaction system including the evaporated material from the target, the surrounding background gas and the laser pulse as shown in Fig. 13. In this figure, the vapor plasma above the target surface is vaporized from the target and subsequently ionized by absorbing laser energy as discussed in Section 2.2.2. It can also contain ionized background gas which, once ionized, is ingested by the plasma. An absorption zone locates in the front of the plasma which can more or less extend back into the plasma and toward the surrounding background gas. The shocked gas corresponds to a layer of background compressed by the outcoming plasma. Absorption of laser radiation can also occur in this layer. Finally the precursor shock separates the ensemble of the plume (containing the vapor plasma and the shocked gas) from the background gas still in the ambient temperature and pressure. Strong interactions can take place between the different parts of the plume. Such interaction can be of mechanical, themal or radiative natures. The expansion of the vapor plasma mechanical compresses the surrounding background gas leading to the shocked gas layer behind the precursor shock. Thermal conduction occurs from the hot vapor plasma to the shocked layer. Finally the radiation emitted by the hot vapor plasma can be absorbed by the surrounding background gas and lead to its heating. The optical property of the background gas is modified consequently by its interaction with the vapor plasma.

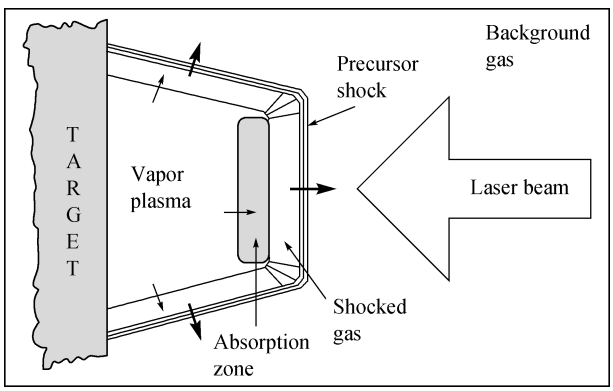

Fig. 13 Schematic representation of the structure of a plasma propagating in a background gas. Reproduced and adapted from Ref. [50], Copyright © 1989 Marcel Dekker Inc.

3.1 Absorption of laser radiation by vapor plume and shocked background

A hot and partially ionized gas, which may correspond to the vapor plume as well as the shocked background gas, absorb the laser radiation principally through inverse bremsstrahlung (IB) (free–free transitions) as well as photoionization (PI) (bound–free transition) [50]. For nanosecond lasers ablation, on the one hand, the photon energy is much smaller than the ionization potential and on the other hand, the laser irradiance is much too small for significant multiphoton absorption to occur. One can consider the total absorption coefficient as contributed by the single photon ionization of excited states (α_{PI}) and inverse bremsstrahlung (α_{IB}). The second is furthermore contributed by electronneutral inverse bremsstrahlung ($\alpha_{IB,e0}$) and electron–ion inverse bremsstrahlung ($\alpha_{IB,ei}$). The total absorption coefficient is thus given in the following form:

$$\alpha_{\rm tot} = \alpha_{PI} + \alpha_{IB,e0} + \alpha_{IB,ei} \tag{23}$$

3.1.1 Absorption by inverse bremsstrahlung

Inverse bremsstrahlung corresponds to absorption by a free electron when its trajectory is modified by passing nearby a heavy particle, a neutral atom or an ion. After such three body collision event, a photon (of wavelength λ) is absorbed by the electron which is accelerated. In the classical electrodynamics the cross section for inverse bremsstrahlung is calculated separately for neutrals, $\sigma_{e,0}^{IB}$, and Z-times ionized ions σ_{eZ}^{IB} due to the different types of interaction forces between the two types of particles and electrons [51]. The absorption coefficient can therefore be written in the following form:

$$\alpha_{IB} = n_0\sigma_{e,0}^{IB} + \sum_{Z=1} n_Z\sigma_{e,Z}^{IB} \tag{24}$$

$$\alpha_{IB,e0}(\lambda) = A_1\lambda^3 n_0 n_e T_e^{3/2}\sigma_{\rm dif}\overline{G_{e0}^{IB}} \tag{25}$$

$$\alpha_{IB,ei}(\lambda) = A_2\lambda^3\left[1-\exp\left(-\frac{hc}{\lambda k_{\rm B}T_e}\right)\right] \cdot \sum_{Z=1}\frac{Z^2 n_Z n_e\overline{G_{eZ}^{IB}}}{\sqrt{T_e}} \tag{26}$$

Here A_1 and A_2 are two constants, and their expression and numerical value in the CGS system of units can be found in Ref. [52]. The corresponding values in the MKS system are respectively 8.61×10^{-19} and 1.37×10^{-27}. T_e is the electron temperature. n_e, n_0, and n_Z stand for respectively the number densities of electrons, neutral atoms and Z-times ionized ions. $\sigma_{\rm dif}$ represents the cross section of electron scattering by a neutral atom, which is in the order of 10^{-20} m^2 for a metallic atom as for a gas atom [53, 54]. $\overline{G_{e0}^{IB}}$ and $\overline{G_{eZ}^{IB}}$ are Gaunt factors and can be expressed in the following forms [55]:

$$\overline{G_{e0}^{IB}} = \left[1+\left(1+\frac{hc}{\lambda k_{\rm B}T_e}\right)^2\right]\exp\left(-\frac{hc}{\lambda k_{\rm B}T_e}\right) \tag{27}$$

$$\overline{G_{eZ}^{IB}} = 1+0.1728\left(\frac{hc}{\lambda E_{\rm H}Z^2}\right)^{1/3}\left(1+\frac{2k_{\rm B}T_e\lambda}{hc}\right) \tag{28}$$

Here $E_{\rm H}$ stands for the hydrogen ionization potential. These two factors take into account the correction of the quantum effect to the used classical calculation of the cross sections. And their value is in general close to 1. Finally the factor $1-\exp\left(-\frac{hc}{\lambda k_{\rm B}T_e}\right)$ in Eq. (26) results

from the effect of stimulated emission.

Equations (25) and (26) can be used to study the behavior of the inverse bremsstrahlung absorption as a function of the electron temperature and the wavelength of the laser radiation. Electron–neutral process, $\alpha_{IB,e0}(\lambda)$, is important only at low temperature for a week ionized plasma [56]. The up limit temperature is in the range of 5 000 K for a metallic plasma such as aluminum vapor, and 10 000 K for a gas such as argon. For higher temperatures, electron–ion process, $\alpha_{IB,ei}(\lambda)$, becomes dominant. Concerning the dependence on laser wavelength, when $h\nu \gg k_{\rm B}T_e, \alpha_{IB}$ varies as λ^3 and when $h\nu \ll k_{\rm B}T_e, \alpha_{IB}$ varies as λ^2. The transition temperature between these two regimes for typical Nd:YAG laser wavelengths are 13 500 K for 1064 nm, 40 500 for 355 nm and 54 100 K for 266 nm. Inverse bremsstrahlung absorption starts with free electrons initially available in the vapor or in the shocked gas. It increases the electron temperature and leads to impact excitation or ionization of the atoms in the plasma. A higher excitation temperature modifies the optical absorption property of the atoms. This aspect will be discussed in the following Subsection. Impact ionization can lead to cascade ionization in the vapor or the gas and increases significantly the ionization degree.

3.1.2 Single photon ionization of excited states

The condition for single photon ionization of excited states can be given by $h\nu > E^k_{\rm ion}$, where $E^k_{\rm ion}$ represents the energy necessary to ionize an atom in its excited state labeled by the principal quantum number k. This energy is equal to the difference between the ionization potential of the atom, $E_{\rm ion}$, and the excitation energy of the state k: $E^k_{\rm ion} = E_{\rm ion} - E_k$. The total absorption due to photoionization can be written as

$$\alpha_{PI} = \sum_Z \sum_k^{\infty} n^k_Z \sigma^{PI}_{k,Z} \tag{29}$$

Here n^k_Z is the number density of the population in the excited state k of the Z-times ionized atoms and $\sigma^{PI}_{k,Z}$ is the cross section of single photon ionization of a Z-times ionized atom from its k excited state. The lowest excited state contributing to the total photoionization depends on the structure of the atom and the wavelength of the laser radiation. In Table 3, we provide the quantum number k and the excitation energy of the lowest excited state concerned with single photon ionization due to the three wavelengths from a Nd:Yag laser for two atoms, aluminum and argon. We can see that for used wavelengths, only excited atoms can be directly photoionized [57, 58]. The needed excitation energies are quite high especially for argon. Such excitation is provided in the plasma by collisional excitation with electrons and can correspond to very high temperatures. According to this model, the absorption coefficient for single photon ionization can be calculated for hydrogenic atoms [59]:

$$\alpha_{PI}(\lambda) = A_2\lambda^3 \left[1 - \exp\left(-\frac{hc}{\lambda k_{\rm B}T_e}\right)\right] \cdot \left[\exp\left(\frac{hc}{\lambda k_{\rm B}T_e}\right) - 1\right] \sum_{Z=1} \frac{Z^2 n_Z n_e \overline{G^{PI}_Z}}{\sqrt{T_e}} \tag{30}$$

with

$$\overline{G^{PI}_Z} = 1 - 0.1728\left(\frac{hc}{\lambda E_{\rm H} Z^2}\right)^{1/3}\left(1 - \frac{2k_{\rm B}T_e\lambda}{hc}\right) - \exp\left(-\frac{hc}{\lambda k_{\rm B}T_e}\right)\left[1 + 0.1728\left(\frac{hc}{\lambda E_{\rm H} Z^2}\right)^{1/3} \cdot \left(1 + \frac{2k_{\rm B}T_e\lambda}{hc}\right)\right] \tag{31}$$

Here A_2 is the same factor as in Eq. (26). $\overline{G^{PI}_Z}$ is the Gaunt factor and $E_{\rm H}$ stands for the hydrogen ionization potential. Eq. (30) can be generalized to non hydrogenic atoms by replacing the Gaunt factor by the Biberman factor [60, 61].

Table 3 The principal quantum number of the lowest excited energy level concerned by single photon ionization and the corresponding excitation energy for two atoms of aluminum and argon excited by the three frequently used wavelengths for LIBS provided by a Nd:YAG laser.

Atom	Aluminum			Argon		
wavelength /nm	1064	355	266	1064	355	266
k	8	3	3	19	6	2
E_k/eV	4.83	3.14	3.14	14.7	12.9	11.5

3.1.3 Relative contributions of IB and PI and the total absorption coefficient

Considering the Gaunt factors are equal to 1 in Eqs. (26) and (30), we get the ratio between the PI and IB processes for the case where the electron–ions dominates the IB process:

$$\frac{\alpha_{PI}}{\alpha_{IB}} = \exp\left(\frac{hc}{\lambda k_{\rm B}T_e}\right) - 1 \tag{32}$$

The ratio shows that when $h\nu \gg k_{\rm B}T_e$, PI is a dominant process, and when $h\nu \ll k_{\rm B}T_e$, IB is the dominant one.

Combing Eqs. (25), (26) and (30), we can write the total absorption coefficient in the form of

$$\alpha_{\rm tot} = A_1\lambda^3 n_0 n_e T_e^{3/2}\sigma_{\rm dif}\overline{G^{IB}_{e0}} + A_2\lambda^3\left[1 - \exp\left(-\frac{hc}{\lambda k_{\rm B}T_e}\right)\right]\sum_{Z=1}\frac{Z^2 n_Z n_e}{\sqrt{T_e}} \cdot \left\{\left[\exp\left(\frac{hc}{\lambda k_{\rm B}T_e}\right) - 1\right]\overline{G^{PI}_Z} + \overline{G^{IB}_{eZ}}\right\} \tag{33}$$

In order to have an insight on the behavior of the total absorption coefficient for typical wavelengths used in

LIBS, we estimate the ratio between the total absorption coefficients at the two wavelengths of 1064 nm and 355 nm for a typical configuration of a shocked argon gas with a pressure of 400 bar and propagating at a velocity of 5 km/s. This ratio, $\frac{\alpha_{\rm tot}(1064)}{\alpha_{\rm tot}(355)}$ reaches 12 for a temperature of 7000 K (0.6 eV). It decreases to 3 at 10 500 K (0.9 eV) and increase rapidly to 21 at 46 000 K (4 eV). This estimation shows that the absorption in the shocked gas is always more efficient for IR than for UV in the range of temperature of typical plasmas produced by laser ablation. Such behavior is consistent with the calculation reported for a carbon plasma expanding in a residual background [62]. This tendency can be understood by the fact that for the range of wavelength considered here and with moderate laser intensity, PI is only efficient from highly excited levels of the atoms through single photon ionization. The PI absorption rate thus increases with the temperature of the gas and decreases with the laser wavelength. Such decrease remains however quite moderate for typical plasma parameters and used ablation wavelengths in LIBS. On the other hand for IB, the absorption is essentially contributed by the electron – neutral process at low gas temperature (below 10 000 K for argon), and becomes dominated by the electron – ion process as soon as the gas starts to be ionized (typically larger than 1% of ionization). The latter rapidly increases as λ^3 for $\lambda \ll hc/(k_{\rm B}T_e)$, and λ^2 for $\lambda \gg hc/(k_{\rm B}T_e)$ according to the discussion in Section 3.1.1 above. For T_e at 20 000 K, the change of wavelength dependence regime takes place around $\lambda = 720$ nm. Therefore for typical LIBS plasma, the total absorption rate of a shocked background gas sensitively increases with the laser wavelength. Consequently, in general, an IR pulse is more strongly coupled to the plasma than a UV pulse.

3.2 Laser-supported absorption waves

Absorption of laser radiation by the plasma which can include vapor plume as well as shocked background gas accelerates the propagation of the plume towards the laser incoming direction and leads to an anisotropic expansion called laser-supported absorption wave (LSAW). In the literature, three major types of LSAW can be distinguished depending on laser irradiance, beam spot size and ambient gas conditions: laser-supported combustion (LSC) waves, laser-supported detonation (LSD) waves, and laser-supported radiation (LSR) waves [50]. The difference in the wave mode arises from the different mechanisms of laser radiation absorption which drives the plasma propagation. In this Section we will present the principal characteristics of the three types of LSAW with the simplified one-dimension model as exposed in Ref. [50], which is suitable for the early stage of plasma expansion.

3.2.1 Laser-supported combustion wave

At low irradiance, laser-supported combustion waves can be produced. As shown in Fig. 14 reproduced from Ref. [50], an absorption zone is found to be localized in the plasma behind the layer of shocked gas which is comprised between the precursor shock (or shockwave) and the plasma. This means that the shocked gas remains transparent for the laser radiation. The last transmits through the shocked gas and is absorbed by the vapor above the target and behind the shocked gas. Consequently, the vapor is efficiently heated to high temperature and pressure as shown in Figs. 14(c) and (d) for the LSC wave. In contrast, the shocked gas remains at low temperature. It is mechanically compressed by the expanding plasma to high pressure and density. The dynamics of the system is maintained by the expansion of the hot plasma. In the transient stage, the absorption wave propagates into the cold and high-pressure shocked gas. The main mechanism of propagation is a radiative transfer from the hot plasma to the cold shocked gas. The high pressure of the shocked gas increases the absorption of the extreme ultraviolet radiation emitted from the plasma. The part of the shocked gas in contact with the plasma becomes rapidly heated, ionized and is ingested by the LSC wave. Its expansion maintains the pressure that drives the propagation of the shockwave.

3.2.2 Laser-supported detonation wave

As the laser irradiance increases, a threshold value can be reached beyond which the shocked gas significantly absorbs the laser radiation. The mode of propagation becomes dominated by the LSD wave. An absorption zone is found just behind the precursor shock inside of the layer of shocked gas [Fig. 14(a)]. No abrupt separation exists between the shocked gas and the vapor plasma. Instead, the pressure, the temperature and the density continuously vary between the vapor plasma and the shocked gas. The propagation of the LSD wave is controlled by the absorption of laser energy by the shocked gas. Higher velocity can be found for the shockwave propagation than in the case of the LSC wave as shown in Fig. 14(b). This implies an accelerated propagation along the laser axis of the plasma in the LSD regime. The consequence of laser absorption by the shocked gas is also a layer of gas with higher pressure, temperature and density than in the vapor behind the shocked gas. The shielding of laser radiation by the shocked gas leads to a vapor with lower pressure and temperature than in the case of the LSC wave as shown in Figs. 14(c) and (d).

3.2.3 Laser-supported radiation wave

At sufficiently high irradiance, the initial heating of the

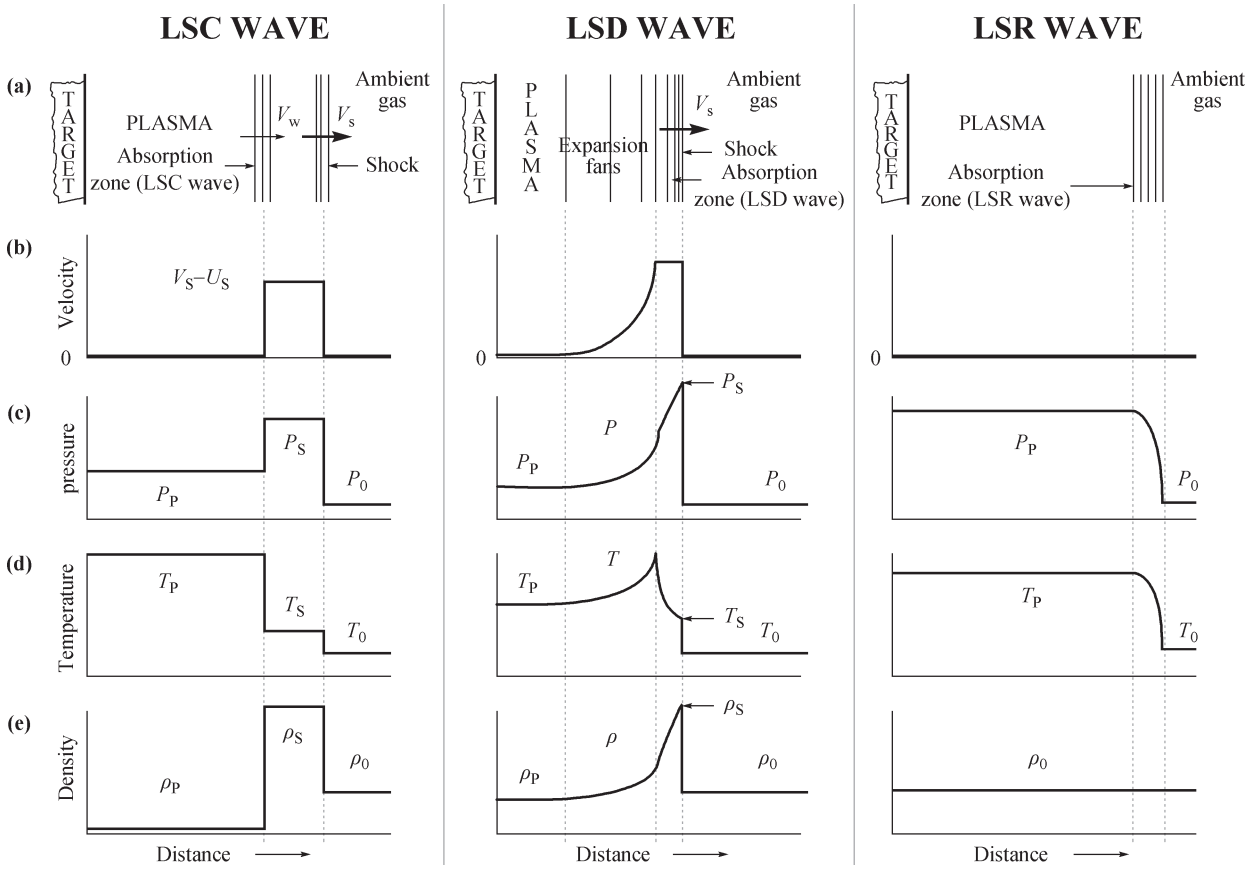

Fig. 14 Illustration of the structures of one-dimensional LSAWs **(a)** and qualitative presentation of the profiles of characteristic parameters of the wave, velocity v **(b)**, pressure P **(c)**, temperature T **(d)**, and density ρ **(e)**. The subscribe P is used for the plasma, S for shocked gas and 0 for the ambient gas. Reproduced from Ref. [50], Copyright © 1989 Marcel Dekker Inc.

ablation vapor leads to a plasma at very high temperature. The extreme ultraviolet radiation emitted from the plasma will be so strong, prior to the arrival of the shockwave, that the ambient gas is heated to high temperature where significant absorption occurs. In the pure LSR regime, the background gas is heated and ionized locally without any change in pressure and density. The absorption wave propagates therefore at the velocity of the light into the background gas until to a distance where the plasma radiation is sufficiently attenuated. As shown in Fig. 14 for LSR wave, the part of the background gas ionized by the plasma radiation is totally ingested by the plasma. A zone of high temperature and high pressure includes the vapor plasma and the ionized background gas.

3.2.4 Transition between LSAW regimes: Effect of irradiance and wavelength

As mentioned above, transition between the different types of LSAW is controlled by the absorption of laser radiation by the vapor and the shocked background gas. According to Eq. (1), the quantity of energy deposited in the plasma by the laser pulse is proportional to the product of the laser irradiance and the absorption coefficient, αl. Since α exhibits strong dependence on laser wavelength λ, I and λ appear therefore as two convenient parameters which provide practical ways to control the regime of LSAW through the control of laser energy deposition in the plasma. Figure 15 reproduced from Ref. [50] shows the characteristic velocities, pressures and temperatures that can be found in different regimes of LSAW. By measuring these characteristic parameters as a function of laser irradiance at given laser wavelength, the irradiance ranges corresponding to each type of LSAW can be determined as shown in Fig. 15(a). It is important to note that in Fig. 15, the irradiance ranges determined for different LSAW regimes are associated to the wavelength of a CO_2 laser at 10.6 μm in the infrared and in the one-atmosphere air background condition. When the wavelength changes, and since the absorption coefficient scales roughly as λ^2 or λ^3 (cf. Section 3.1.3), a correction factor has to be applied in order to find the good indication of irradiance ranges for different regimes of LSAW.

For typical LIBS applications, a Nd:YAG laser is used for ablation with an irradiance in the range of 10 GW/cm^2. If the fundamental of Nd:YAG laser at 1.064 μm is used, a correction factor of 10^2 can be applied to the irradiance scale of Fig. 15 for a rough estimation of the irradiance ranges corresponding to the different LSAW regimes. Such estimation indicates that an

irradiance of 10 GW/cm^2 at 1.064 μm corresponds to 100 MW/cm^2 at 10.6 μm, which is within the irradiance range for the LSD wave. LSD has been observed for a copper plasma induced by a 1.064 μm pulse in an argon background with a laser pulse of irradiance of 7.3 GW/cm^2 [63] in agreement with the above estimation.

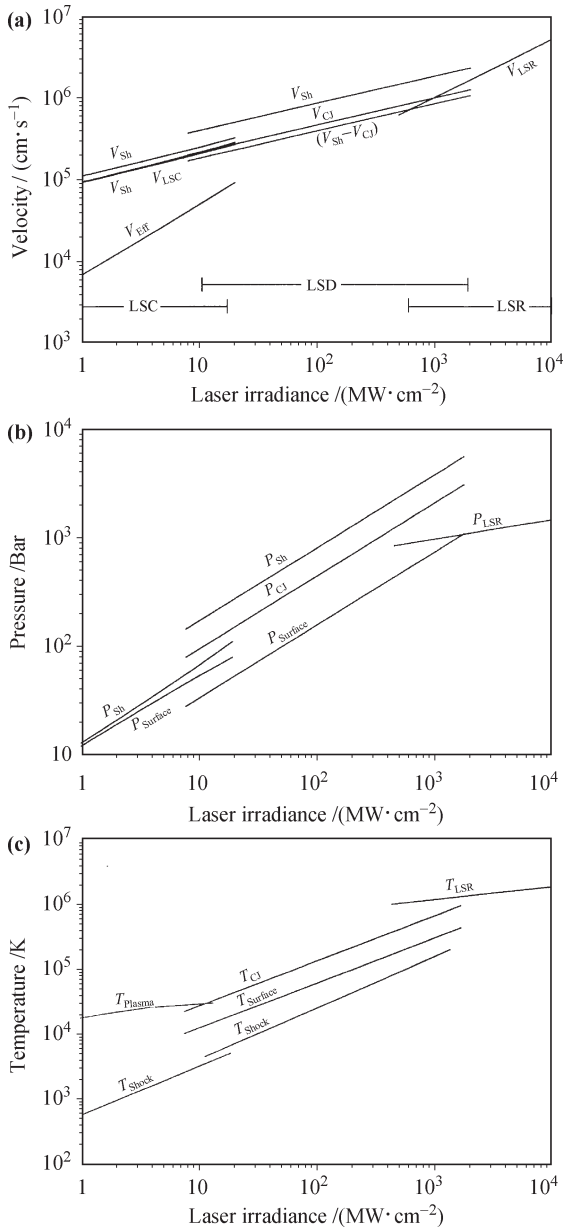

Fig. 15 Characteristic parameters for plasma expansion into a background gas of ambient air as a function of the laser irradiance of a CO_2 laser at 10.6 μm. Different irradiance ranges for the three modes of LSAW are also indicated. Reproduced from Ref. [50], Copyright © 1989 Marcel Dekker Inc.

3.3 Effect of the LSAW on the propagation of the plasma into the background

The practical implications for LIBS of the different modes of LSAW can be discussed according to the understanding elements described above. We see that the energy driving the expansion of a plasma comes from its center in LSC propagation but from its top front in LSD propagation. In other words, in the LSC propagation mode, the vapor plasma pushes the background gas out as described by the piston model; while in the LSD propagation mode, the vapor plasma is pulled away by the accelerated propagation of the shocked gas. Laser absorption by shocked background gas occurs mainly through electron–ion IB process as soon as it becomes ionized as mentioned above. The absorption is thus more efficient for an IR pulse, and much less for a UV one. We can thus expect a secondary breakdown in the layer of shocked gas for IR ablation corresponding to the LSD wave propagation model. For UV ablation at a same level of irradiance, the LSC propagation is expected with a shocked gas layer remaining still transparent and a vapor plasma heated to higher temperature by absorbing the laser radiation. The consequence on the morphology of the plasma is that the LSD wave leads to an elongated form of the plasma due to the accelerated propagation of the shocked gas. While the LSC wave is expected to exhibit a more spherical morphology. We will show in the following Sub-Sections, some results of experimental observation on the propagation of a plasma into a background gas. Emphasis will be the comparison between the behaviors of the LSC and the LSD waves. Experimental controlling parameter of the regimes of LSAW will be laser wavelength and irradiance.

3.3.1 Early stage of plasma expansion

The morphology of the ablation plume is sensitively dependent on the LSAW regime. We have seen above that the propagation velocity of the shock precursor is larger in the LSD regime than in the LSC regime [Fig. 15(a)]. The standard technique for the observation of the early stage expansion of the plasma is time-resolved shadowgraph. Such observation is suitable to show the propagation of the shockwave with high time resolution up to nanosecond [64]. In Figs. 16 and 17, we show time-resolved shadowgraphs of a plasma induced from a nylon target with nanosecond UV (266 nm) and IR (1064 nm) pulses [65]. Laser pulses of 5 ns pulse duration are used with pulse energies of 1, 3, and 5 mJ and a focus spot diameter of 100 μm, which corresponds to a laser fluence of respectively 12.7, 38.1, and 63.7 J/cm^2, and a laser irradiance of respectively 2.5, 7.6, and 12.7 GW/cm^2. In Fig. 16, we can see that the shockwave corresponding to UV ablation exhibits a fairly spherical expansion for all the three used laser energies. Spherical expansion of the shockwave suggests that the LSC wave is the dominant propagation mode for the UV ablation with the used laser irradiances. A localized structure is observed at the top of the shockwave for high irradiances. Such a structure can be due to the direct ionization of the background air by the incident UV laser pulse. The

behavior shown in Fig. 17 for an IR laser pulse is quite different. The observed shadowgraphs of shockwave are significantly elongated toward the laser pulse incoming direction. The elongation is more pronounced at higher irradiance. The resulted shockwave propagation velocity is obviously higher than in the case of UV ablation shown in Fig. 16. These behaviors suggest that the LSD wave is excited for IR ablation with the used laser irradiances [65].

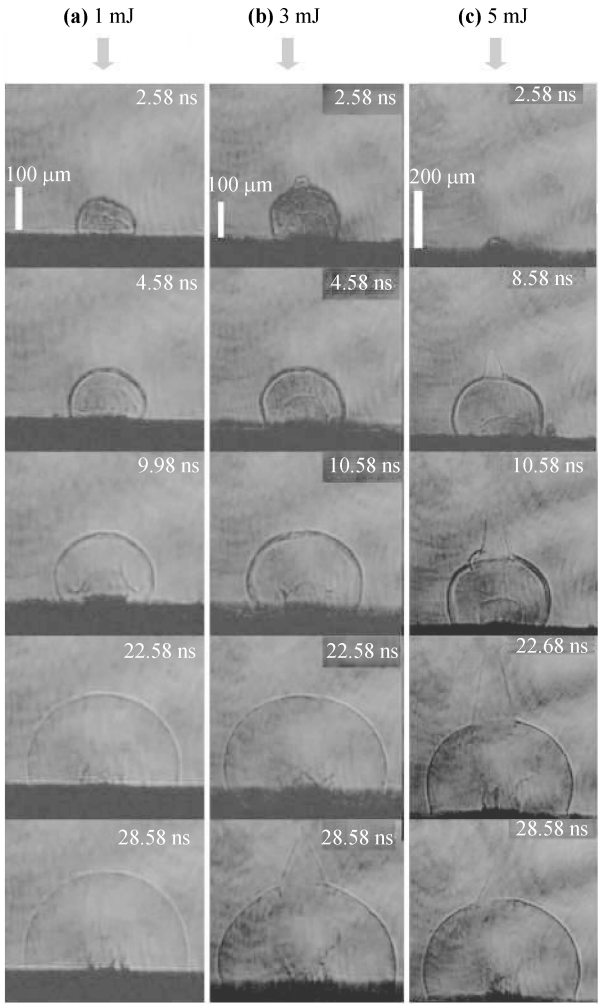

Fig. 16 Shadowgraphs of the plasmas induced on the surface of a nylon sample by a nanosecond UV (266 nm) laser pulse, with pulse energies of 1, 3 and 5 mJ [**(a)**, **(b)** and **(c)**, respectively]. Reproduced from Ref. [65], Copyright © 2009 Elsevier.

3.3.2 Expansion behavior at longer delays

At longer delays, the structure and the evolution of the plasma are resulting from the regime of LSAW at a short delay. At a delay typically longer than 500 ns, the continuum emission from the plasma is sufficiently damped. Time- and space-resolved emission spectroscopy becomes a suitable diagnostics technique to study the structure and the evolution of the plasma [65]. Plasma parameters, such as emission intensity profile, electron density and temperature, can be extracted from the emission

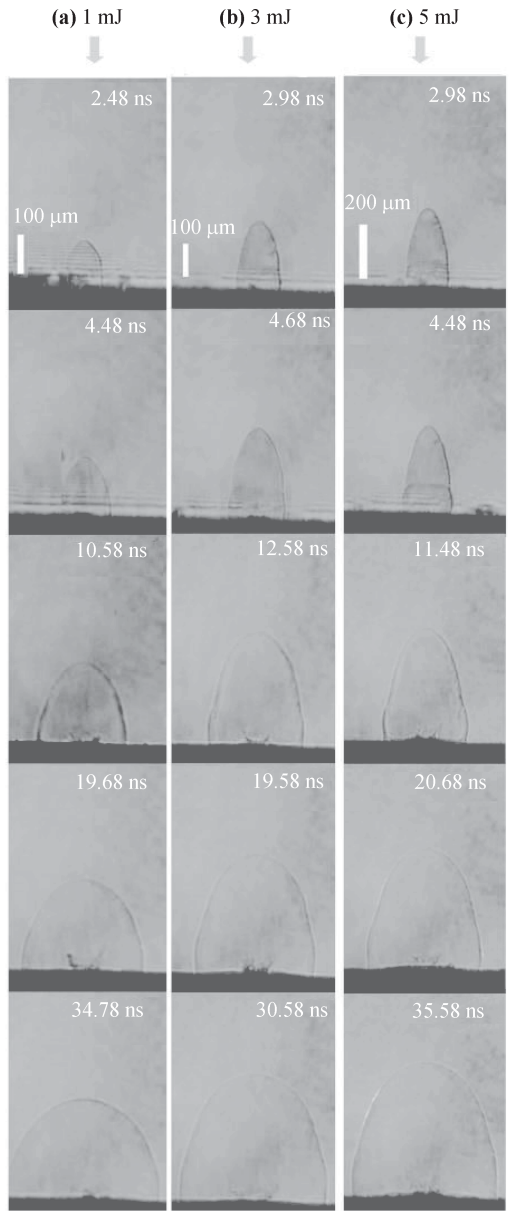

Fig. 17 Shadowgraphs of the plasmas induced on the surface of a nylon sample by a nanosecond IR (1064 nm) laser pulse, with pulse energies of 1, 3 and 5 mJ [**(a)**, **(b)** and **(c)**, respectively]. Reproduced from Ref. [65], Copyright © 2009 Elsevier.

spectra. In Figs. 18, 19 and 20, we show some results reproduced from Ref. [67], which provide a comparison between the plasmas induced from a aluminum target by UV (355 nm) and IR (1064 nm) pluses with an irradiance in the range of 10 GW/cm^2.

In Fig. 18(a), the emission intensity profiles are shown for the aluminum vapor and the background argon gas for ablations with the two wavelengths. We can see for the UV ablation, the Al vapor exhibits more compact and almost immobile axial profiles. While in the case of the IR ablation, the Al vapor is still propagating at investigated delays from 500 ns to 3 μs and presents a larger axial extent than in the case of the UV ablation. The profiles of argon are shown in Fig. 18(b). We can see a larger and propagating emission zone for the IR

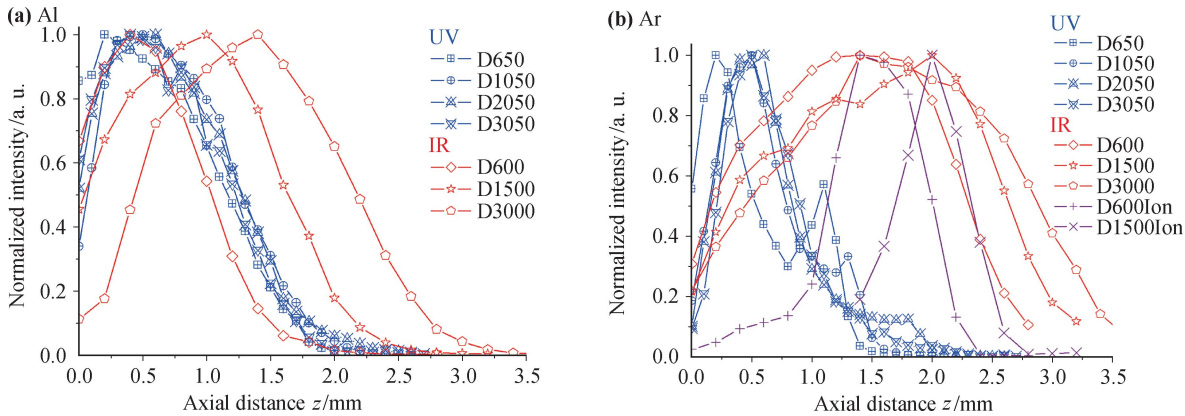

Fig. 18 Line-of-sight integrated normalized emission intensity as a function of the axial distance for the element from the target (aluminum) and the background gas (argon) for different detection delays and the two ablation laser wavelengths. **(a)** Aluminum and **(b)** argon and, for IR ablation, ions of argon (Ar^+). Different investigated delays for UV: 650, 1050, and 3050 ns, and for IR: 600, 1500, and 3000 ns. Reproduced from Ref. [67], Copyright © 2012 The American Institute of Physics.

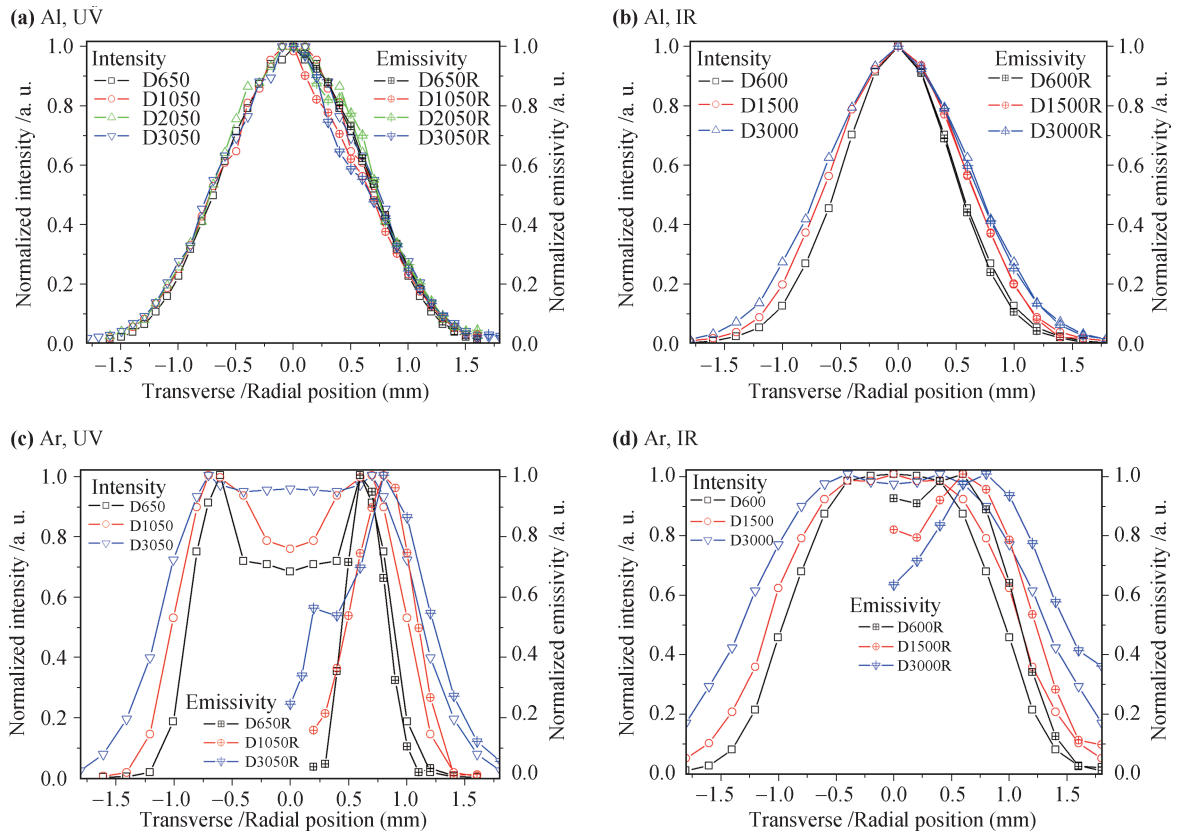

Fig. 19 Normalized transverse line-of-sight integrated intensity profiles and corresponding emissivities obtained with the Abel inversion at the different delays. **(a)** Aluminum for UV ablation; **(b)** Aluminum for IR ablation; **(c)** Argon for UV ablation; **(d)** Argon for IR ablation. Different investigated delays for UV: 650, 1050, and 3050 ns, and for IR: 600, 1500, and 3000 ns. Reproduced from Ref. [67], Copyright © 2012 The American Institute of Physics.

ablation. In the case of the UV ablation, the emission zone of argon is rather localized near the target surface. An important feature to remark is that a distribution of argon ions is observed for the IR ablation on the top front of the plume. Argon ion is not observed for the UV ablation. According to the discussions in Section 3.2, these observations suggest that the UV ablation produces a plasma which propagates with the LSC wave, while the plasma due to the IR ablation is rather characterized by the LSD wave, with a faster axial propagation of the plasma and a well observed layer of ionized background gas. Further observations on the transverse profiles shown in Fig. 19 demonstrate the different behaviors of mixing between the vapor plasma and the background gas. We can see in Fig. 19 that line-of-sight integrated transverse emission intensity profiles and the emissivity profiles obtained from the Abel inversion show an evacuation of the background gas by the vapor plasma for the UV ablation [Fig. 19(c)], while for the IR ablation, the background gas is effectively mixed with the vapor

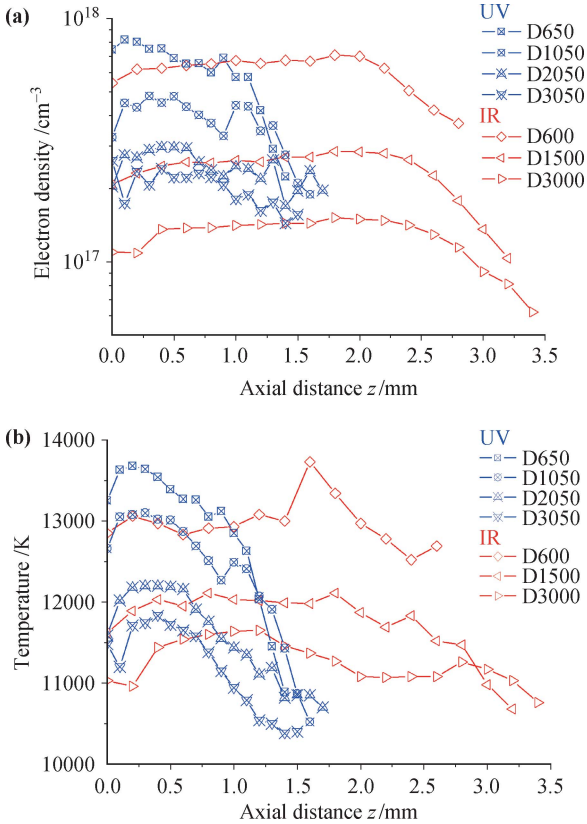

Fig. 20 Axial profiles of electron density **(a)** and temperature **(b)** for UV and IR ablations. Different investigated delays for UV: 650, 1050, and 3050 ns, and for IR: 600, 1500, and 3000 ns. Reproduced from Ref. [67], Copyright © 2012 The American Institute of Physics.

plasma even in the middle of the plume [Fig. 19(d)]. The observed difference in plasma structure and evolution between the UV and the IR ablations shows once again different LSAW regimes. The efficient vapor–gas mixing observed for the IR ablation is not compatible with the piston model, and seems to be specific for the LSD wave propagation mode [66, 67].

Profiles of electron density and temperature are shown in Fig. 20 with a direct comparison between the UV and the IR ablations. A compact, hot and dense plasma is observed for the UV ablation in accordance with the LSC model. For IR ablation in contrast, we can see a plasma with a larger axial extent and slightly lower electron density and temperature than in the case of UV ablation, which is in agreement with the LSD model of plasma propagation. Comparing the emission intensity profiles in Fig 18 and the electron density profiles in Fig. 20, we can clearly identify the contribution of the electrons due to the ionization of the background gas to the total electron density profile of the plasma. These electrons are distributed in the out part of the plasma where the emission from aluminum is much reduced. The consequences of the different regimes of LSAW propagation for UV and IR ablations on the performance of LIBS application are moreover discussed in Refs. [66] and [67] by the authors.

4 Conclusions

The intense development over more than one decade of the LIBS technique makes laser-induced plasma a quite familiar spectroscopic emission source which as we know, exhibits a number of specific and advantageous features compared to other types of conventional emission or absorption sources suitable for spectroscopy. Such features promise numerous potential applications in a wide range of domains. The improvement of the actual performance of the LIBS technique however crucially depends on the deep understanding of the mechanisms involved in the LIBS process which represents, contrarily to a simplistic consideration, a very complex process. In this review paper, we have tried to analyze such complexity by discomposing the process step by step from the arrival of the laser pulse on the surface of a target until the formation of a plasma as light emission source propagating into a background gas. In the description of each involved process, our emphasis is focused on the understanding of the physical phenomenon. We does not have, in this paper, the intention to provide neither a systematic and exhaustive review nor a mathematically rigorous treatment of the laser-induced plasma. Our objective is to provide a comprehensive description of the process with the help of the materials available in the literature and some results recently obtained in our laboratory. Although there is no need of becoming an expert in the physics of laser-induced plasma for starting or continuing to develop or apply LIBS, we believe that a thorough understanding of the ensemble of physical phenomena underlying the technique represents the best insurance of an optimized issue for the development as well as the application of the technique. Providing comprehension elements for understanding step by step what happens in laser-induced plasma is actually our intention in writing this review paper. For readers who want to go deep into more details in the physics of the laser-induced plasmas, this paper can be considered an introduction. The ensemble of the references used in this paper, which are neither exhaustive nor exclusive as mentioned above, can complete the lecture. Finally, great progresses are actually expected for a deeper understanding of the laser-induced plasma as well as for LIBS technique. Review on this field will certainly need to be renewed in a near future.

References and notes

1. J. L. Delcroix and A. Bers, Physique des Plasmas, Paris: InterEditions/CNRS Editions, 1994
2. M. Capitellia, A. Casavola, G. Colonna, and A. De Giacomo, Spectrochim. Acta. B, 2004, 59: 271
3. L. J. Radziemski, Spectrochim. Acta. B, 2002, 57: 1109
4. J. D. Winefordner, I. B. Gornushkin, T. Correll, E. Gibb, B.

W. Smith, and N. Omenetto, J. Anal. At. Spectrom., 2004, 19(9): 1061

5. D. A. Cremers and L. J. Radziemski, Handbook of Laser-Induced Breakdown Spectroscopy, Chichester: Wiley, 2006
6. A. W. Miziolek, V. Palleschi, and I. Schechter (Eds.), Laser-Induced Breakdown Spectroscopy: Fundamentals and Applications, Cambridge: University Press, 2006
7. J. P. Singh and S. N. Thakur, Laser-Induced Breakdown Spectroscopy, Elsevier, 2007
8. R. Noll, Laser-Induced Breakdown Spectroscopy: Fundamentals and Applications, Berlin Heidelberg: Springer-Verlag, 2012
9. F. Brech and L. Cross, Appl. Spectrosc., 1962, 16: 59
10. J. Debras-Guédon and N. Liodec, C.R. Acad. Sci., 1963, 257: 3336
11. D. A. Cremers and L. J. Radziemski, Anal. Chem., 1983, 55(8): 1252
12. D. A. Cremers and R. C. Chinni, Appl. Spectrosc. Rev., 2009, 44(6): 457
13. R. Gaudiuso, M. Dell'Aglio, O. De Pascale, G. S. Senesi, and A. De Giacomo, Sensors, 2010, 10(8): 7434
14. F. C. De Lucia Jr., R. S. Harmon, K. L. McNesby, R. J. Wonkel Jr., and A. W. Miziolek, Appl. Opt., 2003, 42(30): 6148
15. M. Baudelet, L. Guyon, J. Yu, J. P. Wolf, T. Amodeo, E. Fréjafon, and P. Laloi, Appl. Phys. Lett., 2006, 88(6): 063901
16. M. Baudelet, J. Yu, M. Bossu, J. Jovelet, J. P. Wolf, T. Amodeo, E. Fréjafon, and P. Laloi, Appl. Phys. Lett., 2006, 89(16): 163903
17. F. Y. Yueh, A. Kumar, and J. P. Singh, Laser-Induced Breakdown Spectroscopy, Ch. 14, edited by J. P. Singh and S. N. Thakur, Elsevier, 2007
18. V. Juvé, R. Portelli, M. Boueri, M. Baudelet, and J. Yu, Spectrochim. Acta. B, 2008, 63: 1047
19. A. I. Whitehouse, J. Young, I. M. Botheroyd, S. Lawson, C. P. Evans, and J. Wright, Spectrochim. Acta. B, 2001, 56: 821
20. http://msl-scicorner.jpl.nasa.gov/Instruments/ChemCam/
21. J. B. Sirven, B. Sallé, P. Mauchien, J. L. Lacour, S. Maurice, and G. Manhès, J. Anal. At. Spectrom., 2007, 22(12): 1471
22. I. B. Gornushkin and U. Panne, Spectrochim. Acta. B, 2010, 65: 345
23. D. W. Hahn and N. Omenetto, Appl. Spectrosc., 2010, 64(12): 335A
24. E. Gamaly, Phys. Rep., 2011, 508(4 – 5): 91
25. E. Gamaly, Femtosecond Laser-Matter Interactions: Theory, Experiments and Applications, Singapore: Pan Stanford Publishing, 2011
26. M. Fox, Optical Properties of Solids, Oxford: Oxford University Press, 2010
27. N. W. Ashcrotf and N. D. Mermin, Solid State Physics, Philadelphia: CBS Publishing Asia LTD, 1976
28. Ch. Kittel, Introduction to Solid State Physics, John Wiley & Sons Inc., 2005
29. P. Drude, Annalen der Physik, 1900, 1: 566; P. Drude, Annalen der Physik, 1900, 3: 396
30. M. von Allmen and A. Baltter, Laser-Beam Interaction with Materials, Berlin Heidelberg: Springer, 1995
31. American Institute of Physics (AIP) Handbook, 3rd Ed., New York: McGraw-Hill, 1972
32. K. Ujihara, J. Appl. Phys., 1972, 43(5): 2376
33. P. W. Chan, Y. W. Chan, and H. S. Ng, Phys. Lett. A, 1977, 61(3): 151
34. N. Bityurin, B. S. Luk'yanchuk, M. H. Hong, and T. C. Chong, Chem. Rev., 2003, 103(2): 516
35. D. Bäuerle, Laser Processing and Chemistry, 3rd Edition, Berlin: Springer, 2000
36. A. Vogel and V. Venugopalan, Chem. Rev., 2003, 103(2): 577
37. L. Urech and Th. Lippert, Photoablation of Polymer Materials, in Photochemistry and Photophysics of Polymer Materials, Ch. 14, edited by N. S. Allen, Wiley & Sons, 2010
38. A. Bogaerts, Z. Chen, R. Gijbels, and A. Vertes, Spectrochim. Acta. B, 2003, 58: 1867
39. A. Bogaerts and Z. Chen, J. Anal. At. Spectrom., 2004, 19(9): 1169
40. Z. Chen and A. Bogaerts, J. Appl. Phys., 2005, 97(6): 063305
41. A. Bogaerts, Z. Chen, and D. Bleiner, J. Anal. At. Spectrom., 2006, 21(4): 384
42. L. J. Radziemski, and D. A. Cremers (Eds.), Laser-Induced Plasma and Applications, New York: Marcel Dekker Inc., 1989
43. L. Spitzer, Physics of Fully Ionized Gas, London: Interscience Publishers, 1956
44. L. Balazs, R. Gijbels, and A. Vertes, Anal. Chem., 1991, 63(4): 314
45. J. A. M. Van Der Mullen, Spectrochim. Acta. B, 1990, 45(1 – 2): 1
46. J. F. Ready, Effect of High Power Laser Radiation, New York: Academic Press, 1971
47. L. I. Sedov, Similarity and Dimensional Methods in Mechanics, London: Academic Press, 1959
48. N. Arnold, J. Gruber, and J. Heitz, Appl. Phys. A, 1999, 69: S87
49. S. S. Mao, X. L. Mao, R. Greif, and R. E. Russo, Appl. Phys. Lett., 2000, 77(16): 2464
50. R. G. Root, Modeling of Post-Breakdown Phenomena in Laser-Induced Plasmas and Applications, Ch. 2, edited by L. J. Radziemski and D. A. Cremers, New York: Dekker, 1989
51. L. D. Landeau and E. M. Lifshitz, The Classical Theory of Fields, Addison-Wesley, 1962
52. J. Richter, Radiation of hot gases, in Plasma Diagnostics, Ch. 1, edited by W. Lochte-Holtgreven, Amsterdam: North-Holland Publishing Company, 1968
53. R. S. Devoto, Phys. Fluids, 1973, 16(5): 616
54. C. J. Knight, AIAA J., 1979, 17(5): 519
55. S. B. Wen, X. L. Mao, R. Greif, and R. E. Russo, J. Appl. Phys., 2006, 100(5): 053104
56. Ya. B. Zel'dovich and Yu. O. Raizer, Physics of Shock Waves and High-Temperature Hydrodynamic Phenomena, New York: Dover, 2002
57. D. I. Rosen, J. Mitteldorf, G. Kothandaraman, A. N. Pirri, and E. R. Pugh, J. Appl. Phys., 1982, 53(4): 3190
58. G. M. Weyl and D. I. Rosen, Phys. Rev. A, 1985, 31(4): 2300
59. D. H. Menzel and C. L. Pekeris, Mon. Not. R. Astron. Soc., 1935, 96: 77

60. L. M. Biberman and G. E. Norman, Opt. Spectrosc., 1960, 8: 230
61. L. M. Biberman, G. E. Norman, and K. N. Ul'yanov, Opt. Spectrosc., 1961, 10: 297
62. J. Hoffman, T. Moscicki, and Z. Szymanski, Appl. Phys. A, 2011, 104(3): 815
63. X. L. Mao, S. B. Wen, and R. E. Russo, Appl. Surf. Sci., 2007, 253(15): 6316
64. S. B. Wen, X. L. Mao, R. Greif, and R. E. Russo, J. Appl. Phys., 2007, 101(2): 023115
65. M. Boueri, M. Baudelet, J. Yu, X. L. Mao, S. S. Mao, and R. E. Russo, Appl. Surf. Sci., 2009, 255(24): 9566
66. Q. L. Ma, V. Motto-Ros, W. Q. Lei, M. Boueri, X. S. Bai, L. J. Zheng, H. P. Zeng, and J. Yu, Spectrochim. Acta. B, 2010, 65(11): 896
67. Q. L. Ma, V. Motto-Ros, F. Laye, J. Yu, W. Q. Lei, X. S. Bai, L. J. Zheng, and H. P. Zeng, J. Appl. Phys., 2012, 111(5): 053301